Quaternary Science Reviews 58 (2012) 30–55

Contents lists available at SciVerse ScienceDirect

Quaternary Science Reviews

journal homepage: www.elsevier.com/locate/quascirev

Transient subglacial hydrology of a thin ice sheet: insights from the Chasm esker, British Columbia, Canada

Matthew J. Burke, Tracy A. Brennand*, Andrew J. Perkins

Department of Geography, Simon Fraser University, 8888 University Drive, Burnaby, BC, Canada V5A 1S6

ARTICLE INFO

Article history:
Received 3 May 2012
Received in revised form
30 August 2012
Accepted 2 September 2012
Available online

Keywords:
Esker
Canal
Glacial hydrology
Glacial lake outburst flood (GLOF)
Ground-penetrating radar (GPR)
Electrical resistivity tomography (ERT)
Cordilleran Ice Sheet (CIS)

ABSTRACT

Glacier drainage systems are never steady state; instead they fluctuate over time and space in response to variation in water input. In order to improve numerical models of glacier hydrology it is important to fully understand the processes controlling subglacial drainage system evolution, but contemporary ice sheet beds are typically inaccessible. Thus, esker distribution, morphology, and sedimentology have been used to infer the dynamics and hydrology of former ice sheets. However, debate remains as to the processes responsible for esker formation and most theoretical investigations have assumed that they formed due to processes that operated beneath thick ice despite many field investigations to the contrary. We investigate esker formation during the final stages of the thin, inactive, and rapidly decaying Cordilleran Ice Sheet (CIS) in interior British Columbia, Canada. A combination of geomorphological, ground-penetrating radar (GPR) and electrical resistivity tomography (ERT) data suggest esker ridge sedimentary architecture is consistent with synchronous formation during a glacial lake outburst flood (GLOF). These data reveal esker ridge deposition most likely took place within an ice tunnel that evacuated late-waning stage flow, following erosion and partial fill of a broader meltwater corridor. Esker ridge sedimentary architecture reveals this depositional environment was dynamic, reflecting complex interaction between ice thickness, ice structure, ice tunnel geometry, flow conditions, and sediment supply. Under these thin, inactive ice conditions ice tunnel location was initially governed by structural weaknesses in the ice and/or equipotential gradient. Because creep closure rates were low, the ice tunnel evolved through feedbacks between conduit growth via frictional melting/mechanical ice excavation, and conduit closure due to sediment infilling, rather than ice creep. This resulted in a non-uniform ice tunnel that enlarged in an upglacier direction and locally unroofed to form open channels during its final stages. These data suggest that eskers may record unsteady, rather than steady flows in a drainage network and so the assumptions often made when using eskers to inform hydrological components of ice sheet models may not be applicable to all ice sheet settings.

1. Introduction

Relatively recent observations from contemporary ice masses have shown that the glacial hydrologic system is never steady (e.g., Gray et al., 2005; Wingham et al., 2006; Fricker et al., 2007; Bell, 2008; Stearns et al., 2008; Carter et al., 2009; Fricker and Scambos, 2009; Jordan et al., 2010; Bartholomaus et al., 2011; Palmer et al., 2011) and instead glacier drainage systems vary strongly through time in response to changes in water input (Bartholomaus et al., 2011). Because the subglacial drainage system can directly influence ice dynamics it is important to incorporate the processes of subglacial water flow in ice sheet models. However, there are only limited datasets for studying subglacial hydrology because contemporary ice sheet beds are largely inaccessible (Fricker and Scambos, 2009). Most investigations have utilized indirect measurements from GPS and satellites (e.g., Gray et al., 2005; Fricker et al., 2007; Sole et al., 2011), dye tracing (e.g., Nienow et al., 1998; Bingham et al., 2005; Werder et al., 2009), and theoretical glaciology or numerical modelling (e.g., Flowers and Clarke, 2002; Hooke and Fastook, 2007; Boulton et al., 2009; Pimentel and Flowers, 2010; Colgan et al., 2011). However, these studies often assume that changes in subglacial conduit position and geometry are controlled by the balance between frictional melting of the overlying ice (governed by water input to, or generation within, the system) and creep closure due to ice deformation (governed by ice thickness and surface slope). The dynamics, of subglacial hydrologic systems beneath thin ice masses, where creep closure rates are presumably low, is largely

* Corresponding author. Tel.: +1 778 782 3617; fax: +1 778 782 5841.
E-mail address: tabrenna@sfu.ca (T.A. Brennand).

0277-3791/$ – see front matter © 2012 Elsevier Ltd. All rights reserved.
http://dx.doi.org/10.1016/j.quascirev.2012.09.004

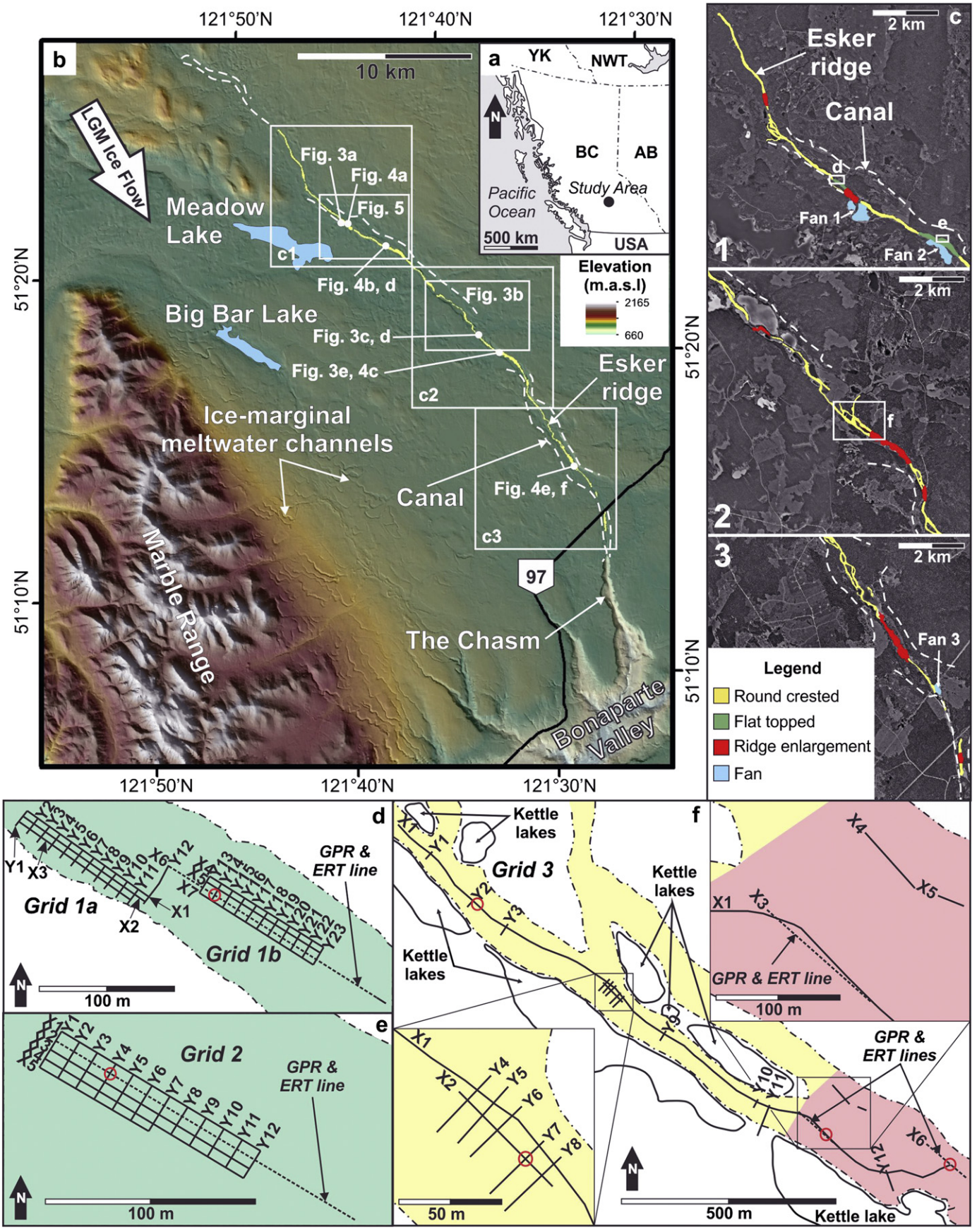

Fig. 1. a) The location of the study area (southern Fraser Plateau) is indicated by the labelled black dot in British Columbia (BC), Canada. b) A hillshaded elevation model of the southern Fraser Plateau (Geobase®). The Chasm esker ridge (yellow line) and canal walls (dashed lines) are labelled. The boxes labelled c1–c3 indicate the location of the panels

ambiguous despite many field investigations of former ice sheet beds that have invoked thin, stagnant ice masses (e.g., Craig, 1964; Shilts, 1984; Aylsworth and Shilts, 1989; Dredge et al., 1999). It is essential that numerical ice sheet models are consistent with the landform record because glaciofluvial landforms have been used to test (e.g., Boulton et al., 2009), or their patterns have been explained by (e.g., Hooke and Fastook, 2007), numerical models. Recent detailed mapping of englacial hydrologic systems suggest that conduit position, flow direction, and geometry can be governed by antecedent structural weaknesses in the ice rather than equipotential gradient, where the ice is thin (e.g., Gulley and Benn, 2007; Benn et al., 2009; Gulley, 2009; Gulley et al., 2009). The ability to directly map englacial hydrologic networks requires the conduits to be at atmospheric pressure for a prolonged period after a fall in discharge (cf. Gulley and Benn, 2007; Benn et al., 2009; Gulley, 2009; Gulley et al., 2009), demonstrating that discharge fluctuations can be out of sync with creep closure rates, at least where the overlying ice is relatively thin. However, major subglacial and englacial channels are inaccessible during conduit formation at contemporary ice masses, making it difficult to investigate conduit dynamics.

Former ice sheet beds present an opportunity to supplement understanding of hydrological processes operating beneath decaying ice sheets through detailed analysis of glaciofluvial landforms, such as eskers. Eskers are the depositional signature of channelized water flow that typically record the infilling of subglacial or englacial conduits (e.g., Brennand, 1994), and subaerial ice-walled channels (e.g., Hebrand and Åmark, 1989; Huddart et al., 1999; Russell et al., 2001; Burke et al., 2008). The distribution, morphology and sedimentology of eskers have been used to infer the dynamics of former ice sheets (e.g., Shilts, 1984; Shreve, 1985; Aylsworth and Shilts, 1989; Clark and Walder, 1994; Dredge et al., 1999; Brennand, 2000; Mäkinen, 2003; Boulton et al., 2009). However, much debate remains as to the processes responsible for esker formation and the timescales over which this takes place (Cummings et al., 2011). Most investigations have assumed eskers record long term hydrological processes at the ice sheet base (e.g., Hooke and Fastook, 2007; Boulton et al., 2007a, 2007b, 2009), whereas rapid esker formation during glacial lake outburst floods (GLOFs) is underplayed (e.g., Brennand, 1994; Brennand and Shaw, 1996). Recent observations from Skeiðarárjökull, Iceland and Bering Glacier, Alaska, on the other hand, demonstrate that eskers can form during single, high magnitude GLOFs (Burke et al., 2008, 2010). This work shows that GLOF eskers have a complex sedimentary architecture including the deposits of large-scale bedforms and ridge-scale (i.e., ridge wide) macroforms that are composed of coarse sand and gravel, with a distinct absence of silt and clay. These characteristics are suggested to be criteria diagnostic of GLOF controls on esker formation (cf. Burke et al., 2010). Given that markedly different interpretations have been proposed for the same esker (e.g., Shreve, 1985; Hooke and Fastook, 2007) it is important we fully understand the processes responsible for esker formation so that eskers can be appropriately used to constrain or test hydrological parameters in ice sheet models. Currently, there is a discrepancy between field investigations that typically suggest esker formation beneath thin, stagnant ice masses (e.g., Craig, 1964; Shilts, 1984; Aylsworth and Shilts, 1989; Dredge et al., 1999) and theoretical studies that invoke conduit dynamics based on thick ice processes (i.e., frictional melting vs. creep closure; e.g. Shreve, 1985; Clark and Walder, 1994; Hooke and Fastook, 2007; Boulton et al., 2009). Furthermore, many field investigations have not been able to assess conduit dynamics because their mandate was geomorphic/glacial geologic mapping, and so they lack detailed data on esker ridge sedimentary architecture (e.g., Shilts, 1984; Aylsworth and Shilts, 1989; Dredge et al., 1999).

In this paper we combine geomorphological and geophysical datasets from an esker in south-central British Columbia (BC), Canada in order to assess the subglacial hydrology of the Cordilleran Ice Sheet (CIS) on a part of the southern Fraser plateau. This esker forms part of a meltwater corridor landsystem that was interpreted to have formed during drainage of an ice-dammed lake (see Section 2.1) (Burke et al., 2012). Because the CIS only reached a maximum thickness of ~600 m in this region (Huntley and Broster, 1994) these data give an insight into conduit dynamics beneath a relatively thin ice sheet (see Section 5.3.1) during ice-dammed lake drainage.

2. Regional setting

The southern Fraser Plateau (located in interior BC, Canada) is dissected at its most southern end by the ~200 m deep Bonaparte Valley and bound by the Marble Range to the southwest (Fig. 1). The plateau surface is relatively flat, till covered and, in places, streamlined (Plouffe et al., 2011). The most recent glaciation of the Fraser Plateau began around 30.5 cal ka BP (Booth et al., 2003) and the CIS reached its maximum extent at around 14–13 cal ka BP when the southern interior of BC was covered by ice up to 600 m thick on the plateaus and 1100 m thick in the valleys (Huntley and Broster, 1994). Rapid decay of the southern sector of the CIS was complete by 10.7 cal ka BP (Clague and James, 2002) and is recorded by meltwater channels, eskers, outwash sediments, hummocky deposits, and glaciolacustrine sediments (Tipper, 1971; Plouffe et al., 2011). The lack of large recessional moraines (cf. Tipper, 1971) is ascribed by Fulton (1991) to ice stagnation and rapid CIS retreat. Eskers on the plateau record the final stages of CIS decay and can give insight into the hydrology of the ice sheet (Perkins et al., 2011a). The largest esker is located upflow from the Chasm (Fig.1), a large bedrock cataract formed through headward erosion from the Bonaparte Valley (Plouffe et al., 2011). The Chasm esker forms part of a meltwater corridor landsystem (Fig. 1) that was identified by Burke et al. (2012).

2.1. Meltwater corridor landsystems on the Fraser Plateau

Burke et al. (2012) identified and investigated the formation of two meltwater corridor landsystems on the Fraser Plateau using a combination of landform mapping from aerial photographs and DEMs, and near surface geophysics on landforms within the corridors. These single-thread meltwater corridors begin abruptly and do not form dendritic networks. Although the two meltwater corridors on the Fraser Plateau have a similar geomorphic signature and inferred evolution, here we only describe the meltwater corridor that leads into the Chasm (Fig. 1a) as this has a direct bearing on Chasm esker formation. The Chasm meltwater corridor is ~45 km long, ~0.25–2.5 km wide, relatively straight, and has an undulating long profile that includes long upslope segments (Fig. 2b). The corridor can be split into upglacier and downglacier sections based upon abrupt changes in geomorphology (Burke et al., 2012). The downglacier section is defined by a ~42 km long and ~0.25–1 km

shown in c. The location of Figs. 3 and 4 are also shown. c) Orthophotographs (Province of British Columbia, 2010) showing zoomed views of the upflow (c1), middle (c2), and downflow (c3) parts of the Chasm esker. The coloured polygons highlight changes in esker morphology and adjacent fans (labelled fans 1–3). The boxes labelled d, e and f indicate the location of panels in d–f. d–f) Maps of survey lines at d) grid 1, e) grid 2, and f) grid 3. Solid lines indicate CO GPR lines alone, whereas the dotted lines locate both GPR and ERT profiles (labelled). Red circles highlight the mid points of CMP GPR surveys. The esker ridge has been colour coded following that shown in legend within panel c. Within f) enlarged views of the boxed areas are shown by the inset panels. (For interpretation of the references to colour in this figure legend, the reader is referred to the web version of this article.)

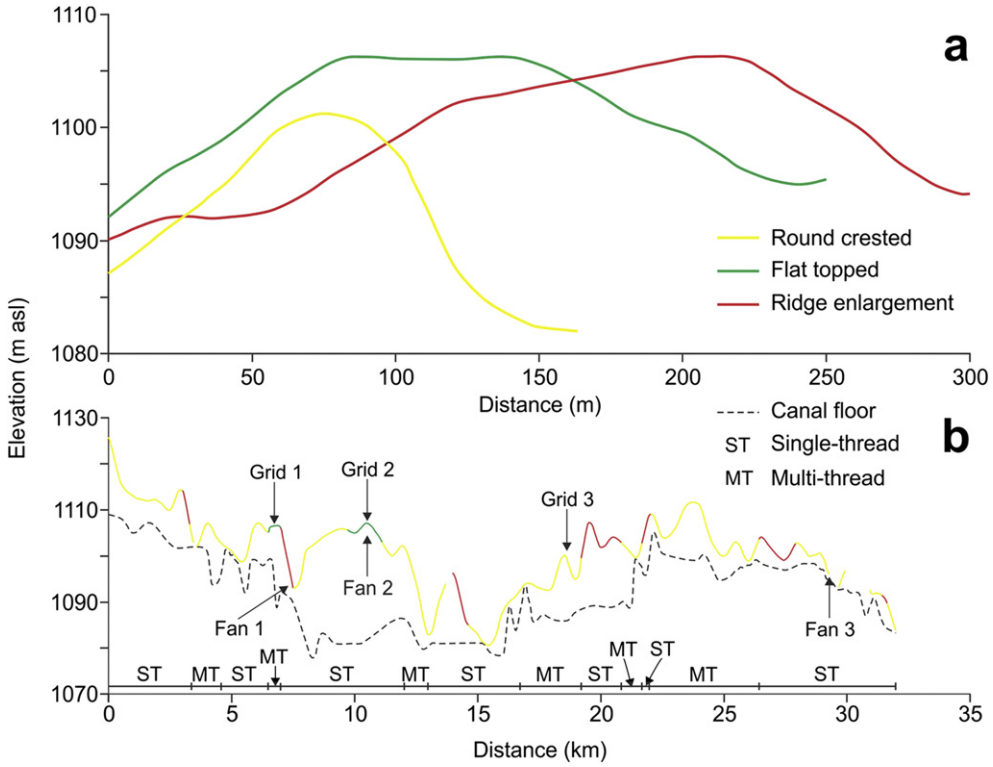

Fig. 2. a) Representative cross profiles of round-crested and flat-topped esker segments, as well as ridge enlargements. b) Long profiles of the esker crestline and canal floor, with GPR grid and fan locations identified by the labelled arrows. The canal floor profile was collected adjacent to the esker where possible. (For interpretation of the references to colour in this figure legend, the reader is referred to the web version of this article.)

wide discontinuous trough that is irregularly cut into the underlying till and/or bedrock (dashed line, Fig. 1a). The head of this trough begins abruptly at an ~0.5 km wide basin that forms a plunge pool with a double horseshoe planform (Burke et al., 2012). The upglacier section of the meltwater corridor is composed of an ~2.5 km wide and ~3 km long zone of scabbed terrain that terminates at the head of the discontinuous trough and contains erosional remnants roughly aligned toward the head of the trough (Burke et al., 2012).

The discontinuous trough component of the meltwater corridor contains a broad fill (based on identification of grid wide deposits within the broad corridor fill) that is composed of gravel sheets and large-scale gravel dunes (Fig. 3a) that are draped by the Chasm esker ridge (Figs. 1 and 3a). Burke et al. (2012) suggest the gravel sheets and gravel dunes were deposited by trough-wide flow and, by extension, that the trough was eroded by this flow to form a tunnel channel. This tunnel channel was suggested to have operated as a large-scale canal (an efficient channel incised down into subglacial sediment (and/or bedrock) and up into the overlying ice (cf. Walder and Fowler, 1994; Ng, 2000)) during tunnel channel formation (Burke et al., 2012). Consequently, we refer to this discontinuous trough as a canal in the rest of this study.

Burke et al. (2012) suggest a simple event sequence for meltwater corridor formation during the drainage of an ice-dammed lake at the corridor head. Initial floodwater propagated as a broad (at least 2.5 km wide) floodwave at the corridor head that then collapsed into efficient canals downglacier where floodwater intersected an antecedent, astronomically-forced ice tunnel (Burke et al., 2012). Intersection of the inefficient floodwave with the ice tunnel was suggested to be like "pulling the plug" on the slowly propagating floodwave, increasing the flow velocity within it, and eroding the scabbed terrain (Burke et al., 2012). Rapid enlargement of the antecedent ice tunnel into a large scale canal is thought to have resulted in rapid evacuation of floodwater and the deposition of the canal-wide fill. Burke et al. (2012) ascribed the lack of reworking and burial by fines of this canal-wide fill to focussing of late, waning-stage floodwaters through a smaller ice tunnel within which the Chasm esker ridge was deposited. However, only limited data from the Chasm esker ridge were presented by Burke et al. (2012). In this study we present detailed data from the Chasm esker ridge and use this to investigate its formation and explore the implications this has for understanding ice tunnel dynamics.

3. Methods

3.1. Landform mapping

The Chasm esker ridge was mapped and its morphology interpreted using stereographic aerial photographs (1:40,000, Province of British Columbia, 2010), digital elevation models (DEMs; 25 m horizontal resolution, 10 m vertical resolution, Geobase®) and ground observations. We qualify esker ridge morphology based upon its long profile, cross profiles, and planform (Figs. 1c and 2) using the following criteria: 1) round-crested ridge segments approximate half cylinders; 2) flat-topped ridge segments approximate half hexagonal prisms; 3) sharp-crested ridge segments approximate triangular prisms; and 4) ridge enlargements are segments where the esker ridge abruptly increases in width (and height in places). Ridge segments are either single-thread or multi-thread (anabranched or subparallel ridges). Lobate, fan-shaped mounds of sediment in close proximity to the esker ridge are mapped as fans (Section 4.1.3).

3.2. Geophysical data collection

Esker ridge sedimentary architecture was investigated using ground-penetrating radar (GPR) and electrical resistivity

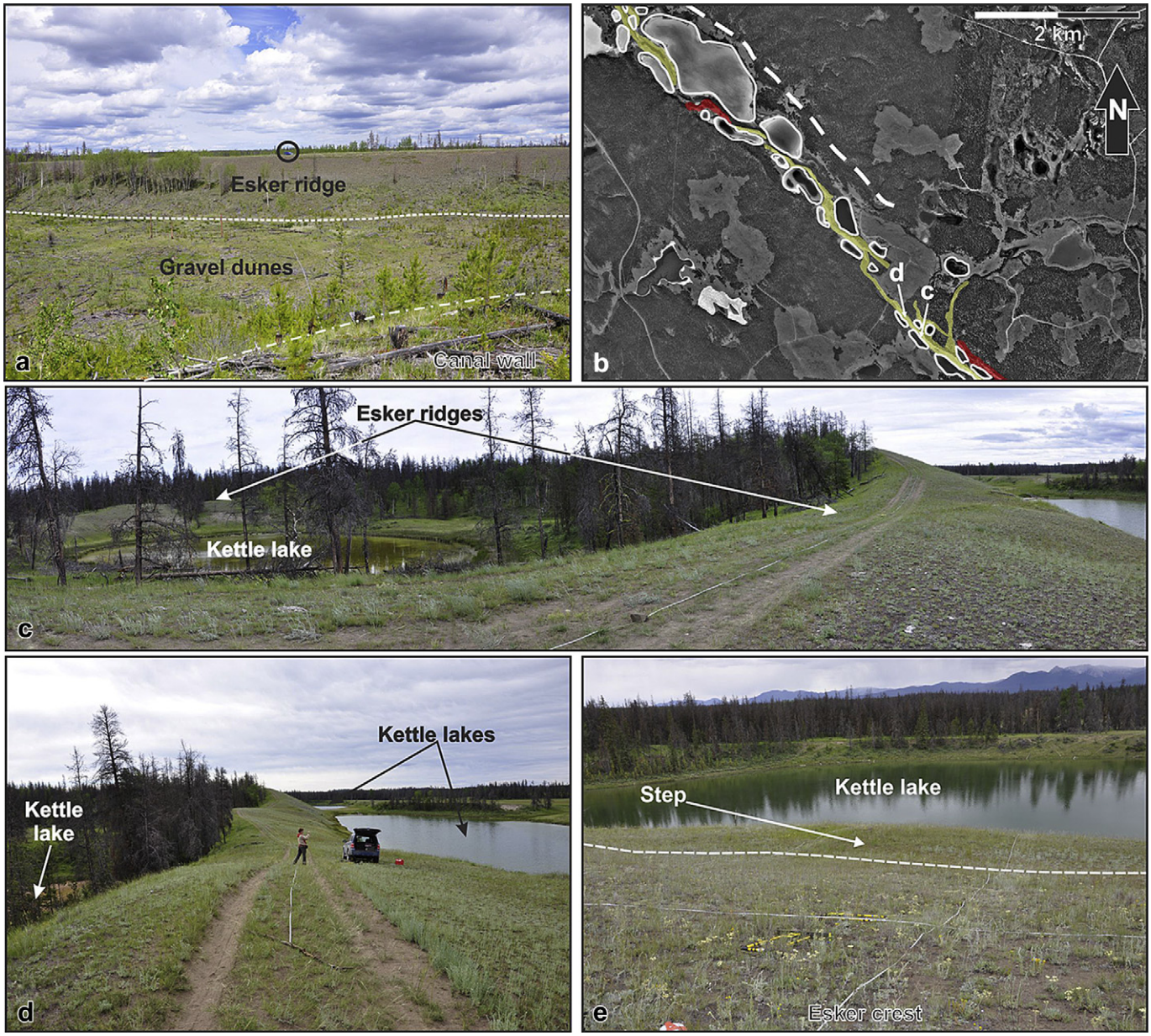

Fig. 3. a) The flat-topped esker segment at grid 1 (photograph was taken from the adjacent canal wall). The esker ridge base is defined by the dashed line, whereas the canal wall edge is defined by the dot-dashed line. Note the vehicle for scale (circled). b) Orthophotograph (Province of British Columbia, 2010) of round-crested esker ridge segments (yellow) and ridge enlargements (red). The white outlines highlight kettle lakes (kettle holes) surrounding the esker ridge. Examples of undulating, round-crested and anabranched esker segments are shown in c) and d). e) Example of a step in the esker ridge flank slope (slump tread) often found along the base of the esker flanks. The dashed line indicates the headward location of the slump tread. Refer to Fig. 1b for the location of each Figure. (For interpretation of the references to colour in this figure caption, the reader is referred to the web version of this article.)

tomography (ERT). A total of ~4.7 km of 100 MHz common offset (CO) GPR lines were collected as three grids along the length of the esker ridge (Fig. 1d–f) using a Sensors and Software Inc. pulseEKKO PRO system. Grid location was primarily determined by site access and suitability to geophysical surveying, but incorporated the key morphological elements of the esker ridge (Fig. 1c and Section 4.1.1). Grids 1 and 2 were located on flat-topped ridge segments, whereas grid 3 was mainly located on the southern round-crested ridge of an anabranched segment and extends onto the downflow ridge enlargement (Fig. 1d–f). Grid lines were regularly spaced where possible, but local site conditions (e.g., presence of trees, esker ridge morphology, etc.) restricted gridded data collection in some places. During CO data collection antennas were kept at a constant separation of 1 m and data were collected in step mode (0.25 m) along the lines to improve ground coupling and trace stacking (32 traces). In order to reduce reflections from offline sources the GPR antennas were co-polarised and perpendicular-broadside to the survey line (Arcone et al., 1995). Nine common mid-point (CMP) profiles, collected at grids 1–3, provided an estimated subsurface average velocity of 0.117 ± 0.009 m/ns, which was used to convert two-way travel time (TWT) into depth and for data processing. Electrical resistivity tomography lines were collected at each grid using an eight channel Advanced Geosciences Inc. (AGI) Super Sting system. Data were collected from a dipole–dipole array (maximum $n = 6$) and all lines had an electrode spacing of 1.5 m, except line X6 of grid 3 where 1 m electrode spacing was employed due to site restrictions. All GPR and ERT lines were surveyed for topographic

variation using a real-time kinematic differential global positioning system (dGPS). Sediment sections and surface materials (Fig. 4) were examined where possible to facilitate geophysical data interpretation.

3.3. Geophysical data processing and inversion

GPR data processing was carried out in REFLEXW v5.6 and included static correction, 'dewow' filtering, bandpass filtering, migration, background removal filtering, application of a gain function, and topographic correction. ERT inversion was carried out in AGI EarthImager 2D v2.40 using the finite element method as a forward model, a smooth model inversion routine, damped transform topographic correction, removal of negative resistivity values and spikes, a minimum voltage filter, and minimum and maximum apparent resistivity filters. Inversion resulted in a maximum of 3.7–8.9% data removal, RMS errors of 1.77–3.10%, and l^2 values (squared and summed differences between apparent and actual resistivity values) of 0.78–3.96.

A steep gravel pit face was located ~2 m upflow from ERT line X2 collected at grid 2. At grid 3, ERT line X3 was collected along the crest of a round-crested segment that became steep flanked (>30°) after ~120 m along the line. The close proximity of the steep pit face at grid 2 and steep esker ridge flanks at grid 3 result in an edge effect within the ERT profiles. This edge effect is represented as anomalously high resistivity values in the ERT profiles associated with the sediment–air interface at the gravel pit wall (grid 2) and steep esker ridge flanks (grid 3). Because individual resistivity values are the average for a three-dimensional block of material around the central point (where the measurement is spatially located), where electrodes are close to the sediment–air interface, the ERT is effectively sampling air, as well as sediment. As the electrical resistance of air is understandably high, this increases the average resistivity values for those points affected by the presence of a sediment–air interface. For the ERT profiles in this manuscript we deem that all resistivity values >13,000 Ω-m are noise associated with this edge effect because: 1) these values are unrealistic for the sand and gravel present in the esker ridge; and 2) this is the

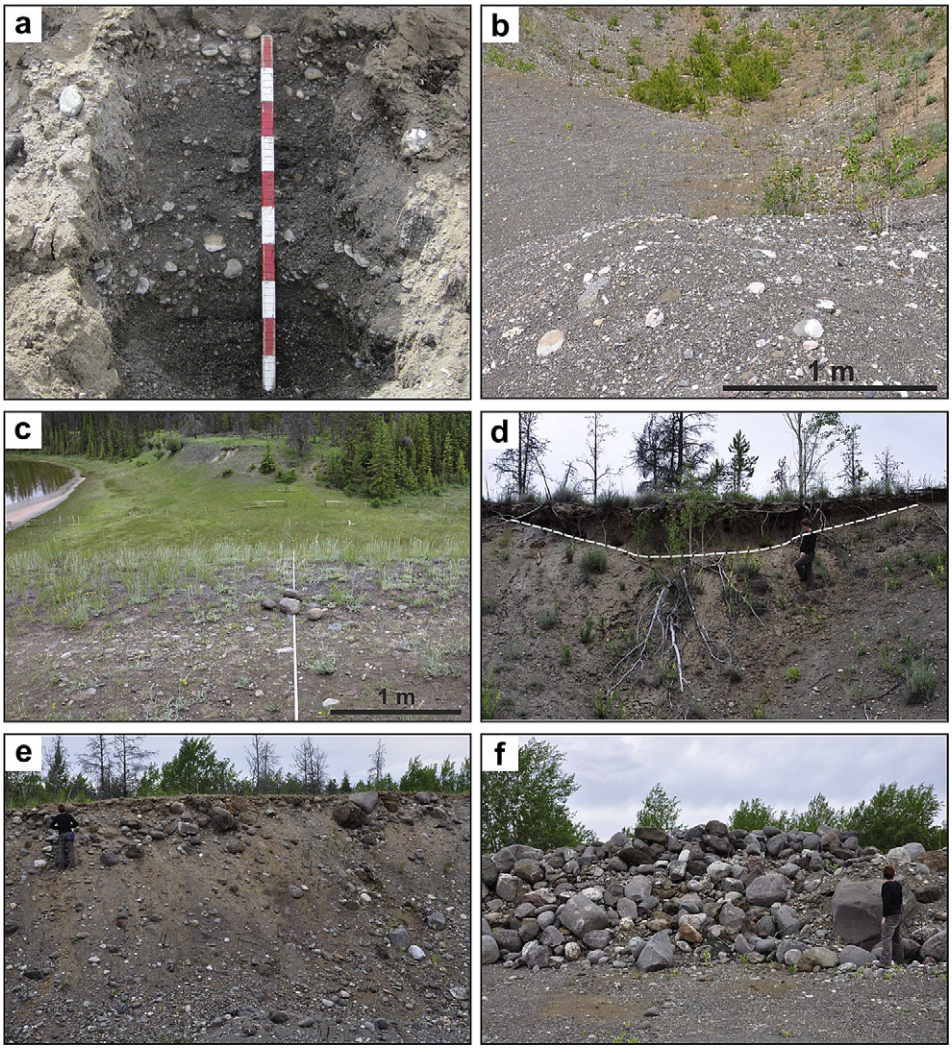

Fig. 4. Material observed within the esker and canal-wide fill. a) Sediment section within the main esker at grid 1, showing that the landform is dominated by sand to pebble-gravel here. Divisions along the 1 m rod are at 0.1 m intervals. b) Sand to pebble-gravel in the base of a gravel pit close to grid 2. d) Sand and pebble- to cobble-gravel at the surface of the main esker at grid 3. c) Fine aeolian sand and silt fill in depressions and drape esker sand and gravel below. The dashed line highlights the base of the fine sediment carapace that is thickest within the base of the depression (the person is ~1.7 m high). e) Sand and cobble- to boulder-gravel (clasts up to 1 m diameter) identified in a gravel pit towards the terminus of the Chasm meltwater corridor (the person is ~1.7 m high). f) Boulder-gravel piled up within a gravel pit at the downglacier end of the Chasm meltwater corridor. Note the person for scale (~1.7 m high). Refer to Fig. 1b for the location of each Figure.

minimum cut off value that can be applied without suggesting the existence of noise where there should be no edge effect.

3.4. Geophysical data interpretation

Resistivity units (labelled RU in Figs. 6c, 9b and 11a, b), inferred to record lithostratigraphic units will be identified from ERT profiles. These lithostratigraphic units will mainly be determined by abrupt changes in material resistance and, where possible, correspondence to GPR profiles. In the GPR profiles, high amplitude, continuous reflections that demarcate the termination of reflections above and below will be identified as bounding surfaces, which will define radar elements within the grids. Only bounding surfaces that can be traced across multiple GPR profiles (where possible) will be picked. Radar elements (labelled in stratigraphic order) will be interpreted based upon the broad style of deposition within the individual radar element (Table 1) and are numbered based on an interpreted depositional event sequence. Where separate radar elements have a similar stratigraphic position, unit geometry, and depositional style these will be grouped into a single depositional event. Offsets in reflections will also be identified because these are typically interpreted as faults associated with post-depositional slumping due to steep esker ridge flanks and removal (melting) of ice support (cf. Fiore et al., 2002; Woodward et al., 2008; Burke et al., 2008, 2010).

4. Results

4.1. Meltwater corridor landsystem geomorphology and sediment texture

Meltwater corridor landsystems on the Fraser Plateau have been identified by Burke et al. (2012). The corridor upglacier of the Chasm is dominated by an erosional canal (cf. Burke et al., 2012) that contains a number of landforms and landform elements that together form the meltwater corridor landsystem. Aside from the erosional canal base, canal-wide deposits, composed of coarse sand to boulder gravel (Fig. 4e, f), are the stratigraphically deepest landform elements (Burke et al., 2012) and are draped by esker ridge segments that are dominated by coarse sand to cobble gravel (Fig. 4a–d). The esker ridge segments (Section 4.1.1) are often closely associated with kettle holes (Section 4.1.2). Although three small fans occur adjacent to the esker ridge, these are interpreted as part of a subsequent proglacial lake landsystem (see Section 5.1).

4.1.1. Esker ridge segments

The Chasm esker ridge is ~32 km long and located within a broader canal (Fig. 1b, c). The esker ridge (central ridge of sand and gravel) is relatively straight (sinuosity ratio of 1.06; esker ridge crestline length divided by straight line length) and semi-continuous, being composed of five aligned esker ridge sections that are ~0.2–15 km long and separated by four ~100–900 m long gaps (Fig. 1). These aligned sections do not form a dendritic network of esker ridge sections (Fig. 1b, c). The Chasm esker ridge (i.e. the five aligned ridge sections) is composed of round-crested segments, flat-topped segments and ridge enlargements (Figs. 1c, 2 and 3). We map no sharp-crested segments and ridge sections do not terminate at fans (see Section 4.1.3). The esker ridge follows an undulating canal long profile that includes long upslope sections, but variations in ridge segment morphology do not correlate to changes in canal floor topography (Fig. 2b).

Round-crested segments occur throughout the esker ridge (76% of the system length) and are single or multi-thread ridges (parallel or anabranched) that have undulating long profiles (Figs. 1c and 3c, d). Round-crested segments can be traced, unbroken, for up to 4.5 km and are ~20–100 m wide (Fig. 2). In places, continuous round-crested segments are interrupted by ridge enlargements that occur sporadically along the esker ridge (18% of the system length) at both single-thread ridges and where multiple ridges join. Ridge enlargements are up to 1.5 km long and ~100–300 m wide (Fig. 2). Flat-topped segments are only identified in two locations (6% of the system length); both are within 12 km of the esker ridge head (Figs. 1c and 3a). They are ~0.45–1.5 km long, and ~80–250 m wide (Fig. 2). Along the base of the esker ridge flanks, regardless of ridge planform, steps (treads) in the esker ridge cross-section are identified (Fig. 3e). These steps have surface textures consistent with the sand and gravel observed on the adjacent esker ridge flank.

Small sediment sections and landform surface texture reveal that round-crested segments and ridge enlargements are composed of coarse sand to cobble-gravel (Fig. 4c), whereas flat topped segments are dominated by coarse sand to pebble-gravel (Fig. 4a, b). However, due to site access, we do not have sufficient data to quantify downflow changes in landform surface texture. Regardless of ridge planform and cross-section, a thin ($\leq$1.5 m thick) carapace of fine sand and silt can be identified in hollows in the landform surface (it is thickest in these hollows, Fig. 4d) and in between crestline undulations. This fine material appears massive in section (Fig. 4d).

4.1.2. Kettle holes

Esker ridges are typically bordered by circular basins (up to ~1.5 km in diameter) that are often filled with lakes (Figs. 1f and 3b–e). Because these depressions are typically restricted to the esker ridge flanks, have circular morphologies, and form closed basins, we interpret them to be kettle holes (cf. Fay, 2002) associated with detachment and melting of ice blocks during CIS decay (Tipper, 1971). These kettle holes are closely associated with the esker ridge, often flanking both sides of the ridge (i.e., surrounding the esker ridge) and separating multiple esker ridge branches in anabranched and multi-thread segments (Fig. 3b–e). Kettle holes are most prevalent along the flanks of round-crested ridge segments and ridge enlargements, and are not present where fans are identified.

4.1.3. Fans

There are three fans located close to the flanks of the Chasm esker ridge at ~7.5 km (fan 1), ~10 km (fan 2) and ~30 km (fan 3) from the head of the esker ridge (Figs. 1c and 5). Fans 1, 2 and 3 are adjacent to a ridge enlargement, a flat-topped ridge segment, and a round-crested ridge segment, respectively (Fig. 1c and 2b). All fans have lobate morphologies (Fig. 5a) and slope angles of $<2^{\circ}$ along fan centreline. Fan 1 dips towards the south, fan 2 to the southeast, and fan 3 to the east. The fans are ~5–15 m higher than the surrounding landscape and, at their highest points, are ~10–20 m lower in elevation than the esker ridge crest at each location. The fans have maximum widths of ~800 m (fan 1), ~350 m (fan 2), and ~300 m (fan 3). No kettle holes or slumps are identified in the fan surfaces or in areas adjacent to the fans. The apex of fans 1 and 2 are consistent with the location of channels that dissect the esker ridge (roughly perpendicular to esker ridge crestline). Fan orientation is consistent with that of the esker-dissecting channels and the fan surfaces dip away from the channel termini (Fig. 5a).

Sections through the fans are rare, but an esker-proximal section through fan 2 (Fig. 5) exposes stratified sand and silt. Lithostratigraphic unit 1 (~3.5 m thick), is composed of massive (~0.04 m thick) and trough cross-laminated (~0.26 m thick) medium to fine sand (palaeoflow direction towards the North), overlain by a rhythmic sequence of laminated fine sand, silt, and (rarely) clay (~3.2 m thick). This rhythmic sequence is punctuated by three beds (~0.01–0.02 m thick) of medium to coarse sand with

Table 1
Summary of radar elements and canal-fill stratigraphy. See Figs. 6c, 9b and 11 for electrical resistivity colour scale (in the web version).

Canal-fill Stratigraphy	Res.[a]	RE Characteristics[b]	RE Interpretation
Post glacial elements[c]	200-900 (RU4)	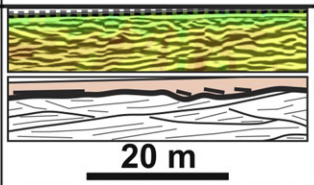 • Low resistivity unit at esker surface, truncating deeper RE • Does not correspond to fine material • Internal reflections are irregular	Gravel pit push
		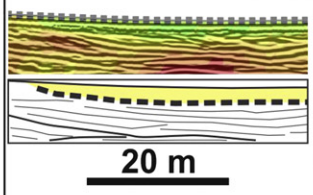 • Thin, low resistivity unit at esker surface, draping deeper RE • Corresponds to fine material at esker surface & in section • Internal reflections obscured by air & groundwaves	Aeloian deposition
	N/A	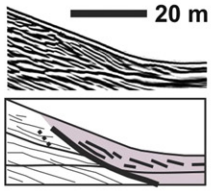 • Asymmetrical & trough-like • Located on esker flanks • Initiate at offset reflections (faults) • Composed of discontinuous & chaotic reflections • Correspond to steps in esker cross-section	Slump
Esker ridge elements	1,500-12,000 (RU3)	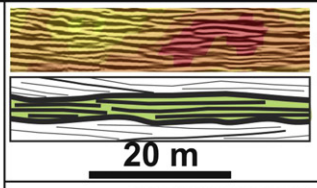 • Stacked with a tabular geometry • Composed of relatively continuous planar reflections that conform to lower bounding surface geometry	Vertical accretion
		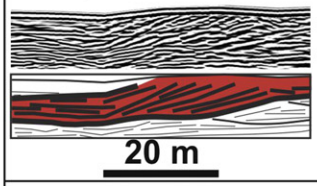 • Upglacier dipping • Composed of reflections that dip upflow at an angle conformable to or greater than that of lower bounding surface	Headward accretion
		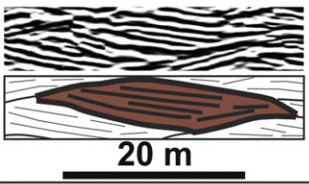 • Downglacier dipping • Composed of reflections that dip downflow at an angle conformable to or greater than that of lower bounding surface	Downflow accretion
		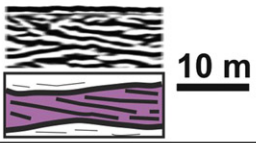 • Tabular geometry • Composed of reflections that dip normal to flow	Lateral accretion
Canal-wide fill elements	2,000-7,500 (RU2)	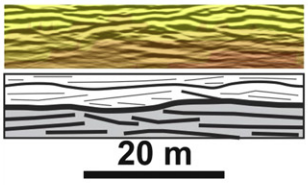 • Grid wide, tabular & high resistivity • Composed of reflections with varied geometries • Have the same characteristics as canal-wide units reported by Burke et al. (2012)	Gravel sheets or dunes

[a]Electrical resistivity in Ω-m
[b]GPR & ERT data (above); interpretation (below) for each RE type. Colour-coding corresponds to that used in Fig. 8a (in the web version).
[c]Post-ice melt.

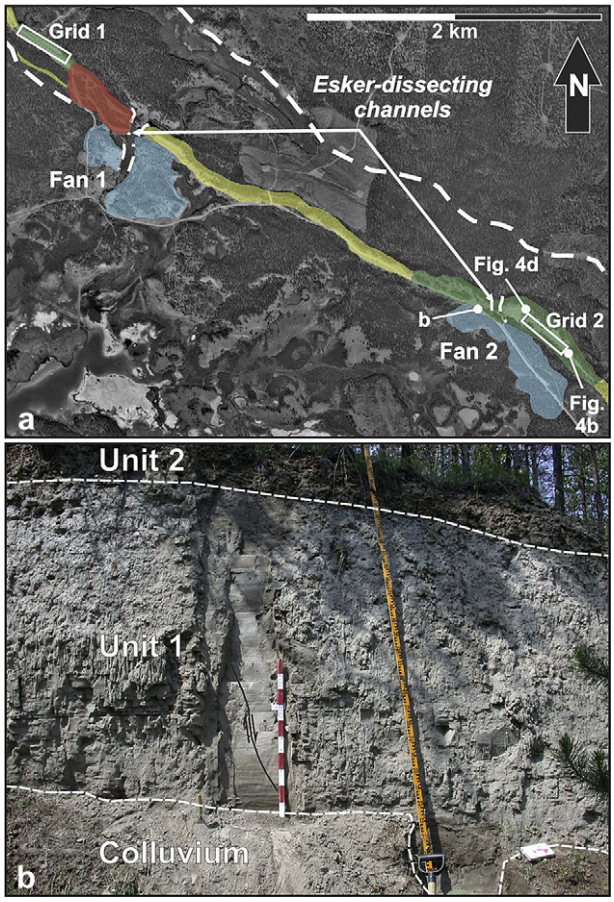

Fig. 5. a) Orthophotograph (Province of British Columbia, 2010) showing the relationship between round-crested esker ridge segments (yellow), flat-topped esker ridge segments (green), an esker ridge enlargement (red), and adjacent fans (blue). The fans have the same numbered labels as in Fig. 1c. The dashed line shows the identified canal wall here. The esker-dissecting channels are labelled and their boundaries marked by the dot-dashed lines. The locations of grid 1, grid 2, and Fig. 4b, d are shown. The arrow labelled b indicates the location of the photograph in b. b) Section through the esker proximal part of fan 2. Unit boundaries are indicated by the white dashed lines. The black line highlights the location of a minor fault, whereas the arrows show displacement direction (only minor). Metre stick is divided into decimetres. (For interpretation of the references to colour in this figure caption, the reader is referred to the web version of this article.)

erosional lower contacts and south-orientated flame structures. Rare normal faults, dipping (71–74°) towards the esker ridge (e.g., arrowed line, Fig. 5b), run from the base of the section up to the top of unit 1 (in some cases), though overall primary bedding appears to be intact. Lithostratigraphic unit 2 (0.48 m thick) drapes lithostratigraphic unit 1, has an irregular lateral geometry and is composed of massive and heavily bioturbated fine sand and silt. The sedimentology of lithostratigraphic unit 1 is consistent with that described in subaqueous fans elsewhere (e.g., Winsemann et al., 2007), though the presence of limited normal faulting suggest these were deposited, at least partially, in contact with ice. The sedimentology of unit 2 is consistent with a record of Holocene aeolian activity that was widespread across the Fraser Plateau (Lian and Huntley, 1999). Fan 1 appears to have a similar texture (sand and silt) to fan 2, but fan 3 was inaccessible.

4.2. Description and interpretation of canal fill, focussing on esker ridge architecture and texture

GPR data are presented as fence diagrams for each grid (Figs. 6a, b, 9a, 12), and ERT profiles are presented two-dimensionally in conjunction with the associated GPR line (Figs. 6c, 9b and 11a, b). All GPR and ERT profiles are presented without any vertical exaggeration. A uniform colour scale has been applied to each ERT profile to allow direct comparison between ERT profiles. All processed and interpreted GPR profiles, as well as animations 1–3, are presented two-dimensionally in the Supplementary material. Below we describe each grid in turn beginning with the most upflow grid and working downflow. For each grid description we first describe the general canal-fill stratigraphy, based primarily on the ERT profiles (Figs. 6c, 7c, 9b, 10b, 11), and then focus upon the radar elements, which we describe in stratigraphic order. These radar elements have been interpreted following the classification outlined in Table 1. All reported reflection dip angles are apparent dip. Faults (offset reflections) are defined by dashed lines. Although faulting is assumed to extend through the full landform thickness, the limited extent that offset reflections can be aligned in the GPR profiles is probably due to difficulties in imaging faulting with GPR (i.e., relative line orientation and GPR resolution) (cf. Fiore et al., 2002; Woodward et al., 2008).

4.2.1. Grid 1

Grid 1 is located at a ~100 m wide, flat-topped esker ridge segment (Figs. 1c, d and 3a) where the landform surface has been anthropogenically modified to some extent. At grid 1a the esker ridge surface is unmodified, whereas grid 1b is located in the base of an abandoned gravel pit where ~2–3 m of material has been excavated from the landform surface (based upon the elevation difference between the unmodified landform surface and the gravel pit base, Fig. 6). Line Y12 crosses a gravel road that appears to have only involved a small amount of landform surface grading. The thickness of this modification is likely less than that of the airwave and groundwave.

An ERT profile was collected along line X6 of grid 1b (Fig. 6c). This ERT profile images deeper than its respective GPR profiles and so allows placement of esker ridge architecture within the broader context of canal-fill stratigraphy (as described and interpreted by Burke et al., 2012; see Section 2.1). ERT values range from ~300 to 7000 Ω-m and the profile can be divided into three lithostratigraphic units (RU1–3, Figs. 6 and 7c). The upper boundary of RU1 is defined by an order of magnitude change in resistivity values below ~1066 m asl, which is higher than the local water table (~1062 m asl). RU1 has a resistivity of ~300–400 Ω-m, consistent with diamicton as measured elsewhere on the Fraser Plateau and in other Quaternary settings (cf. Samouëlian et al., 2005; Pellicer and Gibson, 2011). Because these diamictons are at an elevation similar to till reported by Burke et al. (2012) we interpret this as till, representing the canal base here (Fig. 7c). RU2 (~1066–1082 m asl) has a resistivity of ~2500–7000 Ω-m, consistent with unsaturated sand and gravel (Samouëlian et al., 2005; Pellicer and Gibson, 2011). RU3 (~1082–1092 m asl) has a resistivity of ~1500–4000 Ω-m, consistent with the dominance of pebbly sand and infrequent cobbles observed in the base of the gravel pit, its walls (Fig. 4a), and on the unmodified esker ridge surface at grid 1a. The higher resistivity of RU2 suggests greater gravel content at depth than that observed at the esker ridge surface, the gravel pit base, and in a small sediment section (Fig. 4a).

Radar bounding surfaces define 20 radar elements (labelled A–T in Fig. 6 and referred to as RE-A to RE-T in the text) that can be traced across significant parts of the grid. RE-A is continuous throughout the grid at a maximum depth of ~12 m (~1082 m asl). Although signal attenuation prevents clear imaging of internal reflections and its lower bounding surface, imaged reflections are typically irregular and can dip upflow (e.g., ~20–65 m on line X3, Fig. 6a) or be sub-horizontal (e.g., ~50–80 m, line X5, Fig. 6b). RE-A corresponds to RU2 and its thickness

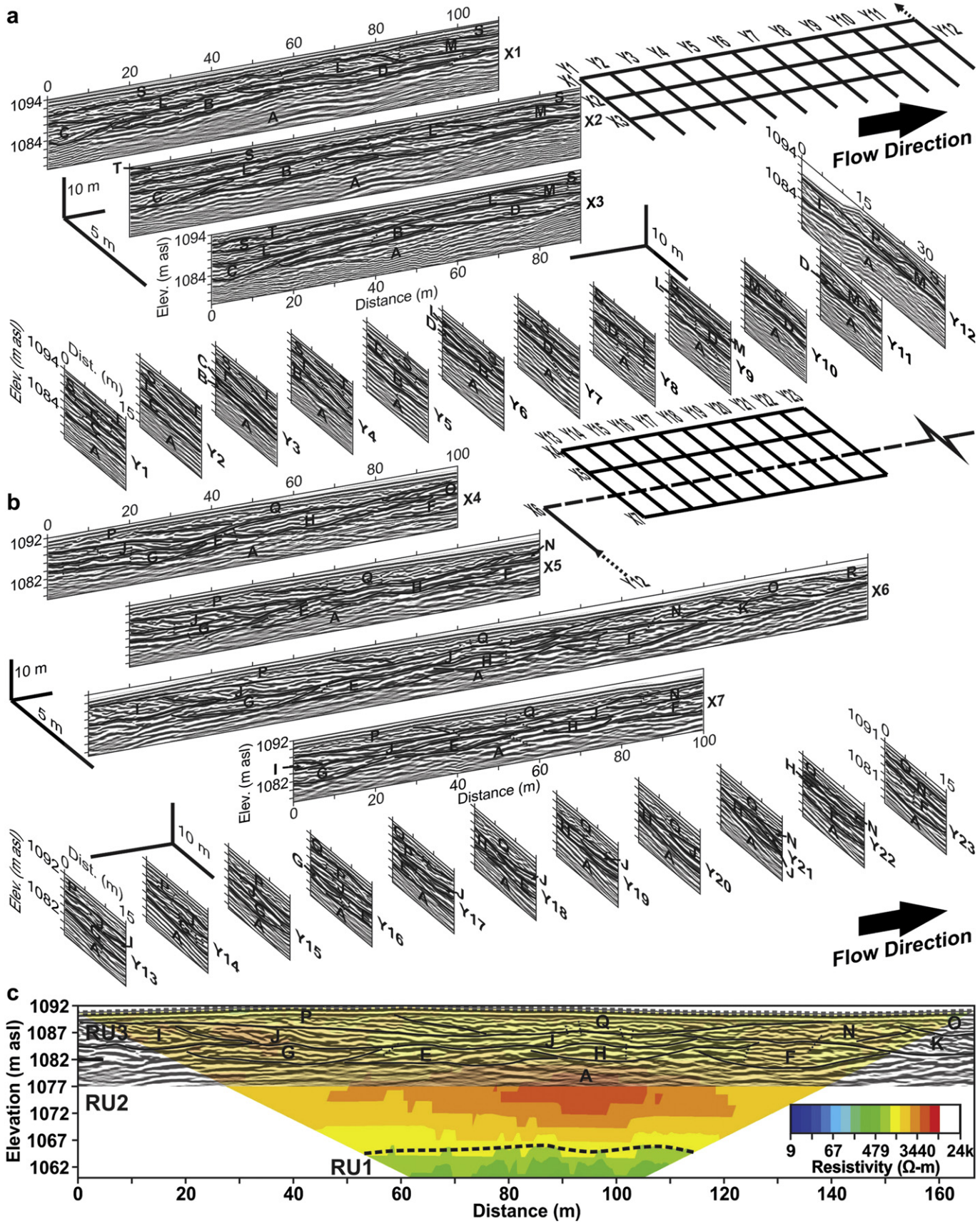

Fig. 6. Fence diagrams of GPR profiles collected at a) grid 1a and b) grid 1b (distance ticks are at 10 m intervals on the *x*-lines and 5 m intervals on the *y*-lines). The data have been processed following the protocol described in Section 3.3. c) Two-dimensional view of part of GPR line X6, grid 1b, overlain on the ERT profile collected at the same location. Inversion resulted in 7.5% data removal, an RMS error of 1.77%, and an I^2 value (squared and summed differences between apparent and actual resistivity values) of 0.78. Lithostratigraphic resistivity units are labelled RU1–3. The bounding surface of RU1 is defined by the dashed line, whereas those of RU2 and RU3 follow radar element bounding surfaces. True relative line orientations are shown in the inset grid maps and Fig. 1d. Radar element bounding surfaces are defined by the bold lines, and radar elements have been labelled (A–T) in order of deposition. Short dotted lines mark offset reflections. (For interpretation of the references to colour in this figure legend, the reader is referred to the web version of this article.)

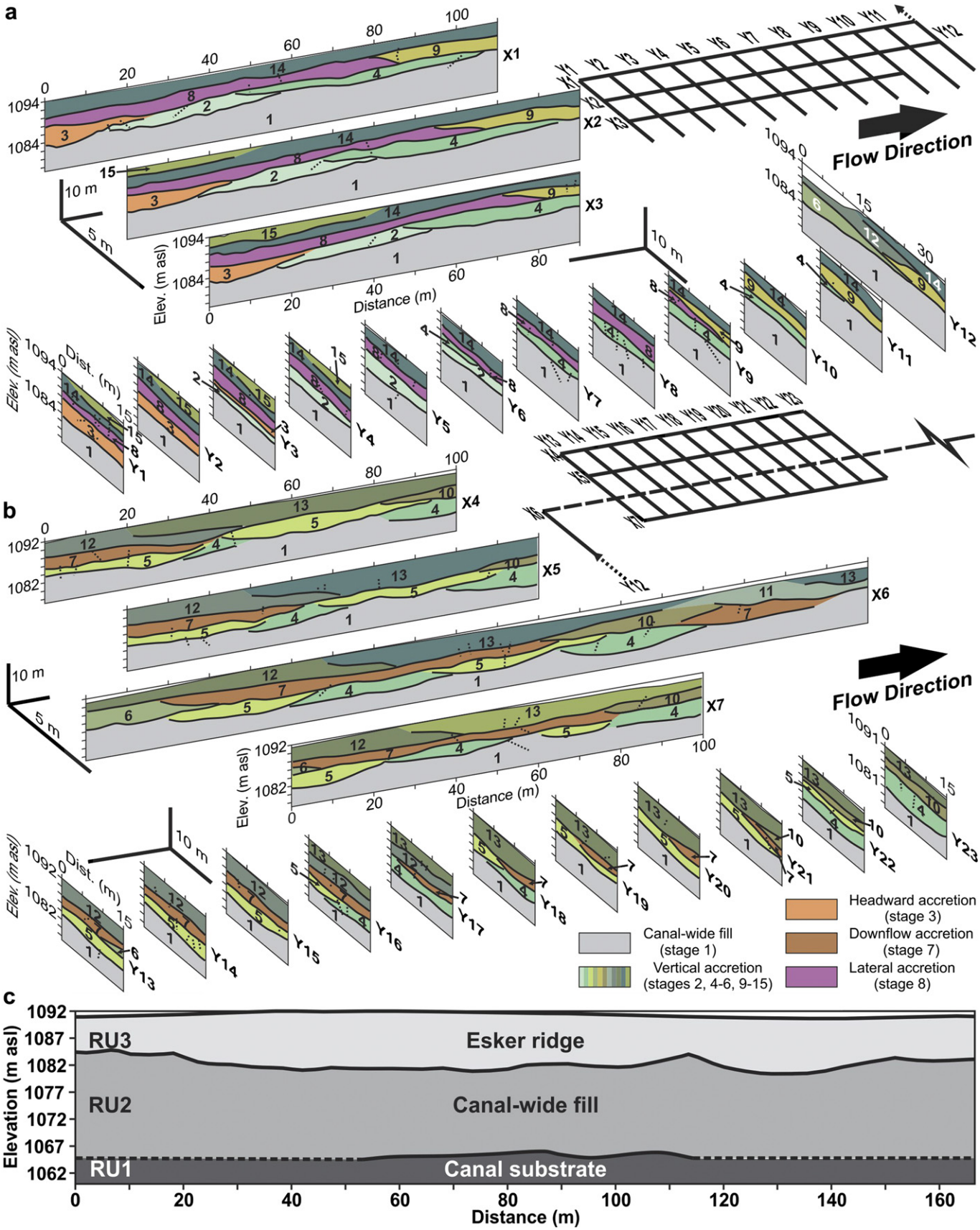

Fig. 7. Fence diagrams of interpreted GPR profiles collected at a) grid 1a and b) grid 1b (distance ticks are at 10 m intervals on the *x*-lines and 5 m intervals on the *y*-lines). True relative line orientations are shown in the inset grid maps and Fig. 1d. Radar elements have been colour-coded based upon the broad style of deposition, using the criteria outlined in Table 1. These colours correspond to those in the legend (bottom right). The radar elements have been numbered (1–15) in order of deposition. Refer to animation 1 (see supplementary data) for an animation of depositional ordering. Short dotted lines mark faults. c) Lithostratigraphic interpretation of ERT profile collected at line X6. Lithostratigraphic units are labelled RU1–3. The dashed lines mark inferred unit boundaries outside of the areas imaged by the GPR and ERT profiles. (For interpretation of the references to colour in this figure legend, the reader is referred to the web version of this article.)

(assuming RE-A is the full thickness of the higher resistivity material in the ERT profile) and elevation correspond to that reported for canal-wide fill here (stage 1, Fig. 7) that is composed of gravel sheets and dunes (cf. Burke et al., 2012). Consequently, RU2 is interpreted as canal-wide fill (Table 1, Fig. 7c). Thus, the stratigraphically higher RE-B to RE-T are interpreted as esker ridge sediments (Fig. 7c).

RE-B to RE-H are typically ~2–6 m thick concave-up, lenticular, cross-cutting elements that are ~12–50 m long in flow-parallel lines and tabular in flow-perpendicular lines (e.g., RE-B, lines Y3–Y6, Fig. 6a). Although the lower bounding surfaces of RE-B to RE-H (stages 2–5, Fig. 7a, b) can conform to reflections within RE-A (e.g., ~40–80 m on line X1, Fig. 6a), they typically truncate reflections in deeper radar elements and so are mainly erosional (e.g., RE-F and RE-H at ~110–120 m on line X6, Fig. 6b). Internal reflections within the RE-B and RE-D to RE-H are fairly continuous and either onlap (e.g., RE-G, line X6, Fig. 6b) or are parallel to (e.g., RE-H, line X4, Fig. 6b) the lower bounding surface, consistent with vertical accretion (stages 2, 4 and 5, Fig. 7a, b and Table 1) of gravel sheets (e.g., Heinz and Aigner, 2003; Wooldridge and Hickin, 2005). In contrast, RE-C is dominated by upflow-dipping reflections (up to 15° from horizontal) that are concordant to that of the lower bounding surface at the downflow end of the radar element. RE-C records headward accretion of gravel sheets (Table 1) (Wooldridge and Hickin, 2005) on the stoss side of the truncated RE-B (stage 3, Fig. 7a).

RE-I to RE-M (stages 6–9, Fig. 7a, b), are typically thinner than RE-B to RE-H (~2–5 m) and more laterally extensive in flow-parallel lines, forming up to ~105 m long tabular radar elements (e.g., RE-J, line X6, Fig. 6b). Because these radar elements truncate deeper reflections they have erosional lower bounding surfaces (e.g., RE-L at ~25–80 m line X1, Fig. 6a). However the internal reflection geometry of RE-I to RE-M is inconsistent. RE-I and RE-M contain reflections subhorizontal to the lower bounding surface, recording vertical accretion (Table 1) of gravel sheets (stages 6 and 9, Fig. 7a, b). The lower bounding surfaces of RE-J and RE-K, on the other hand, are downlapped by downflow-dipping (~10° from horizontal) reflections that grade into sub-horizontal reflections in RE-K (e.g., ~115–145 m, line X6, Fig. 6b). These record downflow accretion (Table 1) of gravel sheets on the lee side of earlier deposits (Wooldridge and Hickin, 2005) (stage 7, Fig. 7b). RE-L is composed of reflections that are sub-horizontal in flow-parallel lines, and dip across flow (up to 10° from horizontal) in flow-perpendicular lines (e.g., line Y3, Fig. 6a), consistent with lateral (Table 1) gravel sheet accretion (cf. Wooldridge and Hickin, 2005; Kostic and Aigner, 2007) (stage 8, Fig. 7a). RE-O and RE-P form stacked concave-up, lenticular radar elements; the lower bounding surfaces of which truncate deeper reflections (erosional). RE-O and RE-P are composed of sub-horizontal reflections that onlap their lower bounding surface (Fig. 6b), recording vertical accretion (Table 1) of gravel sheets (stages 10–11, Fig. 7b).

RE-S is a tabular radar element that is continuous throughout grid 1a (Fig. 6a). It's lower bounding surface is erosional, as it truncates deeper reflections, and the element contains sub-horizontal reflections that drape the lower bounding surface (Fig. 6a), recording laterally extensive vertical accretion (Table 1) of gravel sheets (stage 14, Fig. 7a). RE-T is an elongate trough (e.g., lines X3 and Y3, Fig. 6a), the lower bounding surface of which, truncates reflections within RE-S. RE-T is composed of irregular, but subhorizontal reflections that onlap the lower bounding surface and record vertical accretion of gravel sheets during the final stage of esker ridge deposition here (stage 15, Fig. 7a).

Offset reflections can be traced throughout all radar elements, but are most common in flow-perpendicular lines. Offsets in reflections can be continuously aligned for up to ~6 m (e.g., at ~100 m on line X6, Fig. 6b). However, these reflection offsets do not result in significant distortion of primary reflection geometry. Offset reflections are interpreted as faults associated with post-depositional slumping due to steep esker ridge flanks and removal (melting) of ice support (cf. Fiore et al., 2002; Woodward et al., 2008; Burke et al., 2008, 2010).

In summary, grid 1 records canal-wide fill (cf. Burke et al., 2012) throughout the grid, followed by esker ridge deposition and post-depositional esker ridge reworking (animation 1; Fig. 7c). Initial esker ridge deposits form primarily stacked radar elements that mainly record vertical accretion, though some upflow, downflow, and lateral accretion is also present (Fig. 8a). However, primary radar element geometry is no longer apparent as depositional stages are disconnected by periods of erosion and so the imaged radar elements are presumably remnants of more extensive deposits. The final stages of esker ridge deposition are recorded by laterally extensive (across the full extent of grid 1a), vertically accreting radar elements that result in the development of the flat-topped morphology of the ridge. The dominance of offset reflections in

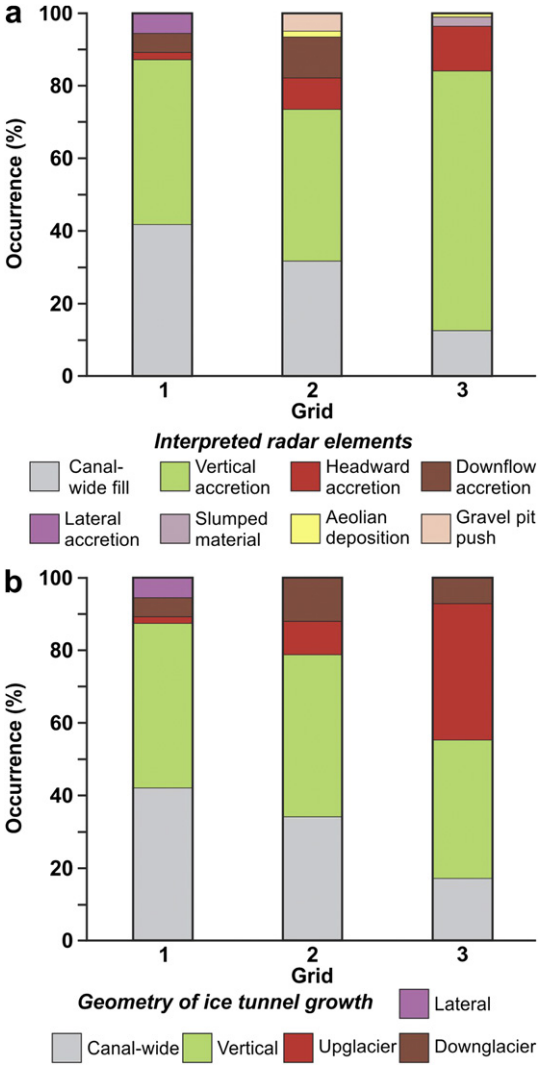

Fig. 8. Histograms showing the occurrence (%) of: a) accretion types (individual radar elements were interpreted following the criteria outlined in Table 1); and b) the geometry of ice tunnel growth inferred from lithostratigraphic architecture within each grid. (For interpretation of the references to colour in this figure legend, the reader is referred to the web version of this article.)

flow perpendicular lines indicates most post-depositional slumping was associated with removal (melting) of lateral ice support.

4.2.2. Grid 2

Grid 2 is located at a ~200 m wide, flat-topped esker ridge segment immediately downflow from an inactive gravel pit (Fig. 1). Although the grid is not located within the gravel pit, it appears that a small amount of surface reworking has taken place, based on the presence of a ridge of pushed sand parallel to flow parallel GPR lines from ~30 m onward.

Resistivity values from an ERT profile collected along line X2 (Fig. 9b) range from ~120 to 22,000 Ω-m, though the highest resistivity values (>13,000 Ω-m) are associated with an edge effect from the steep gravel pit wall just upflow of the grid (Section 3.3). This ERT profile images deeper than its respective GPR profile and so allows placement of esker ridge architecture within the broader context of canal-fill stratigraphy (as described and interpreted by Burke et al., 2012; see Section 2.1). The ERT profile can be divided into four lithostratigraphic units (RU1–4). The upper boundary of RU1 is associated with an order of magnitude change in resistivity

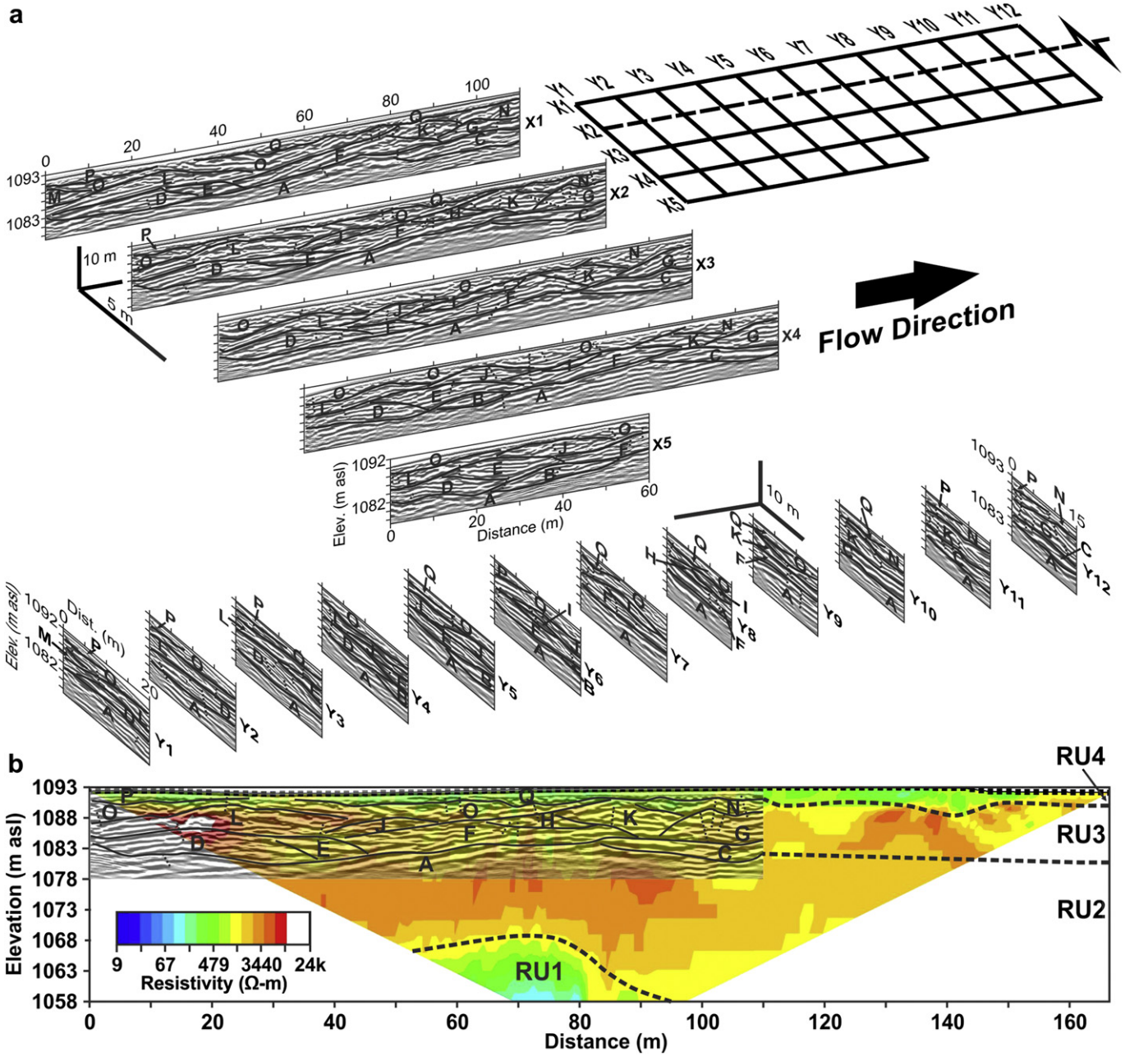

Fig. 9. a) Fence diagram of GPR profiles collected at grid 2 (distance ticks are at 10 m intervals on the *x*-lines and 5 m intervals on the *y*-lines). The data have been processed following the protocol described in Section 3.3. b) Two-dimensional view of GPR line X2, grid 2, overlain on the ERT profile collected at the same location. Inversion resulted in 7.8% data removal, an RMS error of 3.98%, and an l^2 value of 3.96. Lithostratigraphic resistivity units are labelled RU1–4 and their bounding surfaces are indicated by the dashed lines. Where the bounding surfaces of RU2–4 overlap the GPR profile their bounding surfaces follow those of the radar elements. True relative line orientations are shown in the inset grid maps and Fig. 1e. Radar element bounding surfaces are defined by the bold lines and radar elements have been labelled (A–Q) in order of deposition. Short dotted lines mark offset reflections. (For interpretation of the references to colour in this figure legend, the reader is referred to the web version of this article.)

values from ~300–400 Ω-m (RU1) to ~2000–7000 Ω-m (RU2). The upper boundary of RU1 is at an elevation of ~1068 m asl, which is higher than the local water table (~1063 m asl, based on the relative DEM elevation of nearby lakes as seen on orthoimages). Consequently, the low resistivity of RU1 is consistent with the presence of diamicton (cf. Samouëlian et al., 2005; Pellicer and Gibson, 2011), which we interpret as till because it is at an elevation similar to till reported by Burke et al. (2012) that forms the canal base (Fig. 10b). RU2 has a resistivity of ~2000–7000 Ω-m, consistent with unsaturated sand and gravel (Samouëlian et al., 2005; Pellicer and Gibson, 2011). The resistivity of RU3 (~1500–12,000 Ω-m) corresponds to sand and gravel observed in the back-sloped gravel pit immediately upflow from the grid (Fig. 4d) and on the esker ridge surface at the downflow end of grid 2 (Fig. 4b). Low resistivity materials (~200–900 Ω-m) close to the landform surface form RU4, though the thickness of this unit is likely exaggerated somewhat because ERT does not have the vertical resolution to image sharp boundaries. At the upflow end of the grid (up to ~30 m on flow-parallel lines) the esker ridge surface is dominated by fine sands and a decimetre thick unit of fine sands can be seen to fill troughs in the gravel pit upflow from the grid (Fig. 4d). The resistivity of RU4 is similar to that reported

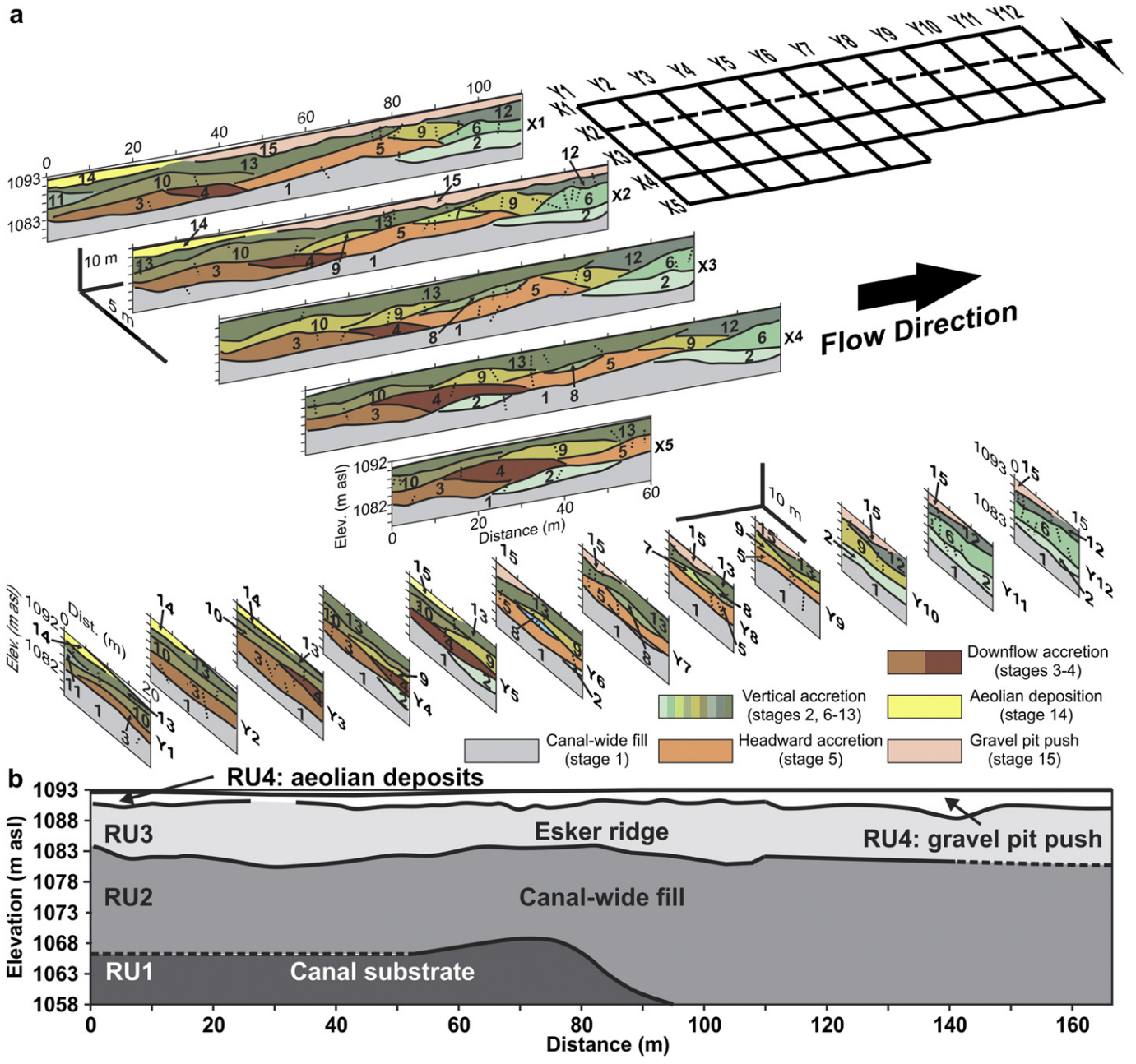

Fig. 10. a) Fence diagram of interpreted GPR profiles collected at grid 2 (distance ticks are at 10 m intervals in the *x*-lines and 5 m intervals in the *y*-lines). True relative line orientations are shown in the inset grid maps and Fig. 1e. Radar elements have been colour-coded based upon the broad style of deposition, using the criteria outlined in Table 1. These colours correspond to those in legend (bottom right). The radar elements have been numbered (1–15) in order of deposition. Refer to animation 2 (see supplementary data) for an animation of depositional ordering. Short dotted lines mark faults. b) Lithostratigraphic interpretation of ERT profile collected at line X2. Lithostratigraphic units are labelled RU1–4. The dashed lines mark inferred unit boundaries outside of the areas imaged by the GPR and ERT profiles. (For interpretation of the references to colour in this figure legend, the reader is referred to the web version of this article.)

for aeolian deposits measured elsewhere on the Fraser Plateau (Perkins et al., 2011b).

Radar bounding surfaces define 17 radar elements (labelled A–Q on Fig. 9a and referred to as RE-A to RE-Q in the text). RE-A is continuous throughout the grid at a maximum depth of ~12 m (~1081 m asl), though signal attenuation prevents clear imaging of internal reflections and its lower bounding surface. Where internal reflections are imaged these are typically irregular and can dip upflow (e.g., ~40–70 m of line X2, Fig. 9a), downflow (e.g., ~20 m of line X2, Fig. 9a) or be sub-horizontal (e.g., 60–90 m of line X3, Fig. 9a). RE-A corresponds to RU2 (Fig. 9b), assuming RE-A extends for the full thickness of the RU2. Because its stratigraphic position, vertical thickness, and internal characteristics are similar to RE-A and RU2 in grid 1 (Fig. 6), and the elevation of its upper bounding surface is similar to that of the canal floor (Fig. 2b) we interpret RE-A at grid 2 as canal-wide fill (Table 1; stage 1, Fig. 10a, b) similar to that reported by Burke et al. (2012). Consequently, RE-B to RE-O are interpreted as esker ridge sediments (Fig. 10b) (RE-P and RE-Q are interpreted as aeolian sediment and gravel pit push, respectively).

RE-B and RE-C form ~3–5 m thick convexo-concave lenticular radar elements, the lower bounding surfaces of which typically truncate reflections within RE-A (e.g., line X4, Fig. 9a) and so are erosional. Internal reflections within RE-B and RE-C are sub-horizontal in flow-parallel and flow-perpendicular lines (Fig. 9a), recording vertical accretion (Table 1; stage 2, Fig. 10a) of gravel sheets (e.g., Heinz and Aigner, 2003; Wooldridge and Hickin, 2005). RE-D to RE-G have a convex-up, mound-like geometry (up to 7 m thick and ~20–40 m long) with lower bounding surfaces that, because they truncate deeper reflections, are erosional (e.g. line X5, Fig. 9a). Internally, these radar elements have varied reflection geometries. RE-D and RE-E are dominated by downflow-dipping reflections (up to ~10° from horizontal; e.g., line X5, Fig. 9a) that are conformable to the upper bounding surface, but onlap the lower bounding surface. These radar elements are consistent with downflow aggradation (Table 1; stages 3–4, Fig. 10a) of gravel dunes (cf. Kostic and Aigner, 2007). RE-F is composed of stacked, upflow-dipping reflections (<10° from horizontal) that downlap the lower bounding surface (e.g., ~50–60 m, line X1, Fig. 9a) and record headward accretion (Table 1; stage 5, Fig. 10a) of gravel sheets (e.g., Wooldridge and Hickin, 2005) onto the stoss side of a high point in the upper bounding surface of RE-A. RE-G is composed of discontinuous, subhorizontal reflections that drape the erosional lower bounding surface (e.g., line X3, Fig. 9a) and record vertical accretion (Table 1) of gravel sheets (stages 6, Fig. 10a).

RE-H and RE-I are <3 m thick concave-up, trough-like radar elements, the lower bounding surfaces of which are erosional because they truncate deeper reflections. Internal reflections are typically subhorizontal and either onlap (e.g., RE-I in line X3, Fig. 9a) or drape (e.g., RE-H in line X2, Fig. 9a) the lower bounding surface. These radar element geometries and internal characteristics are consistent with vertical accretion (Table 1; stages 7–8, Fig. 10a) within scour-and-fill elements (cf. Wooldridge and Hickin, 2005; Kostic and Aigner, 2007).

RE-J to RE-M are convexo-concave, lenticular radar elements (up to 4 m thick) with lower bounding surfaces that truncate deeper reflections. These erosional lower bounding surfaces are typically draped (e.g., RE-L in line X3, Fig. 9a) or onlapped (e.g., RE-K in line X3, Fig. 9a) by subhorizontal reflections. RE-J to RE-M record irregular vertical accretion of gravel sheets (stages 9–11, Fig. 10a).

The final stages of esker ridge deposition are recorded by RE-N and RE-O, which are concave-up radar elements that extend for up to ~90 m long in flow-parallel lines and the full width of the grid in flow-perpendicular lines (Fig. 9a). Their lower bounding surfaces truncate deeper radar elements (e.g., RE-O in line X3, Fig. 9a) and so are erosional. Internal reflections are subhorizontal and typically onlap the lower bounding surface (e.g., at ~20–60 m in line X3, Fig. 9a), recording extensive vertical accretion (Table 1) of gravel sheets that form the flat-topped ridge morphology (stages 12–13, Fig. 10a).

RE-P and RE-Q are the stratigraphically shallowest radar elements that correspond to RU4 in the ERT profile (Fig. 9b). RE-P can only be identified at the upflow end of the grid (i.e., at ~0–30 m in lines X1 and X2, Fig. 9a) where its lower bounding surface drapes deeper radar elements. RE-Q is more extensive and has an irregular lower bounding surface that truncates reflections beneath (e.g., at ~60–80 m on line X1, Fig. 9a). Given these radar elements are shallow, internal reflections are poorly imaged because the elements are largely obscured by the airwave and groundwave, but are typically discontinuous and irregular. The low resistivity values of RU4 in the ERT profile (Fig. 9b) suggest the presence of fine sand (cf. Samouëlian et al., 2005; Pellicer and Gibson, 2011). Because the location and thickness of RE-P corresponds to that of massive fine sand at the landform surface and in the gravel pit immediately upflow from the grid (Fig. 4d), we interpret this radar element as recording aeolian deposition (Table 1) within hollows in the landform surface (stage 14, Fig. 10a). Such Holocene aeolian deposits are extensive across the Fraser Plateau (cf. Lian and Huntley, 1999) and this interpretation is consistent with resistivity measurements of other aeolian deposits on the Fraser Plateau (Perkins et al., 2011b). Although the landform surface at the location of RE-Q is not composed of fine sand, its location corresponds to that of a ridge of pushed sand that indicates the landform surface has been reworked here during gravel pit development. Consequently, RE-Q is interpreted to record gravel pit push (Table 1) following esker ridge and aeolian deposition (stage 15, Fig. 10a). Because surface esker material has been reworked and loosened, its pore spaces are susceptible to infiltration of fine sediment during rainfall, lowering its resistivity.

Offset reflections can be traced throughout all radar elements, but are most common in flow-perpendicular lines. Offsets in reflections can be continuously aligned for up to ~7 m (e.g., at ~42 m on line X4, Fig. 9a). However, these reflection offsets do not result in significant distortion of primary reflection geometry. Offset reflections are interpreted as faults associated with post-depositional slumping due to steep esker ridge flanks and removal (melting) of ice support (cf. Fiore et al., 2002; Burke et al., 2008, 2010; Woodward et al., 2008).

In summary, grid 2 records canal-wide fill (cf. Burke et al., 2012) throughout the grid, followed by esker ridge deposition, aeolian sedimentation, and post-depositional reworking (animation 2; Fig. 10b). Most esker ridge radar elements have either a convex-up and mound-like geometry, or a convexo-concave and lenticular geometry. These radar elements record downflow accretion of large-scale gravel dunes, followed by irregular vertical and headward gravel sheet accretion in hollows (Fig. 8a). However, depositional stages are typically separated by periods of erosion and so primary radar element geometry is no longer apparent. The final stages of esker ridge deposition are recorded by laterally extensive (across the full extent of grid 2), vertically-accreting radar elements that result in the development of the flat-topped ridge morphology. The dominance of offset reflections in flow-perpendicular lines indicates most post-depositional slumping was associated with removal (melting) of lateral ice support. Following esker ridge formation, the landform was draped by aeolian sand (at least at the upflow end of the grid) and the near surface of the landform has been anthropogenically reworked at the downflow part of the grid.

4.2.3. Grid 3

Grid 3 is located at a ~1.5 km long round-crested esker ridge segment that becomes enlarged downflow where anabranched ridges (separated by kettle holes) join (Figs. 1f and 3c). Geophysical surveys were conducted on the southern main ridge of the anabranched section, and extend downflow onto the ridge enlargement. Two ERT profiles were collected: X3 is located just upflow from, and onto, the head of the ridge enlargement (Fig. 11a), and X6 is located entirely on the ridge enlargement (Fig. 11b). These ERT profiles image deeper than their respective GPR profiles and so allow placement of esker ridge architecture within the broader context of canal-fill stratigraphy (as described and interpreted by Burke et al., 2012; see Section 2.1). Resistivity values at X3 are ~9–24,500 Ω-m though the highest resistivity values (>13,000 Ω-m) are associated with an edge effect from the steep flank of the ridge from ~120 m along the line (Section 3.3). The resistivity values at X6 are 171–7664 Ω-m. The ERT profiles can be divided into four lithostratigraphic units (RU1–4, Fig. 11). There is an order of magnitude change in resistivity from ~9–400 Ω-m in RU1 to ~2000–7500 Ω-m in RU2. The upper boundary of RU1 is irregular and is at an elevation of ~1060–1072 m asl, which does not correspond to that of the local water table (~1068 m asl, as indicated by the elevation of flanking kettle lakes measured by dGPS during data collection). The resistivity of RU1 (~9–400 Ω-m) is consistent with the presence of diamicton (cf. Samouëlian et al., 2005; Pellicer and Gibson, 2011). Because this diamicton has similar resistivity characteristics to that at grids 1 and 2 we interpret it as till and the canal base (Fig. 11c, d). RU2 has a resistivity of ~1500–7500 Ω-m in both lines, consistent with values expected for sand and gravel (Samouëlian et al., 2005; Pellicer and Gibson, 2011), with the lower resistivity values of material at the base of RU2 being attributed to saturation below the water table. RU3 has a resistivity of ~2000–11,000 Ω-m at X3 and ~2000–7000 Ω-m at X6, which corresponds to sand and cobble-gravel observed along the landform surface at ~0–60 m of line X3 and along the esker ridge flanks (Fig. 4c). The higher resistivity values in RU3 here, compared to

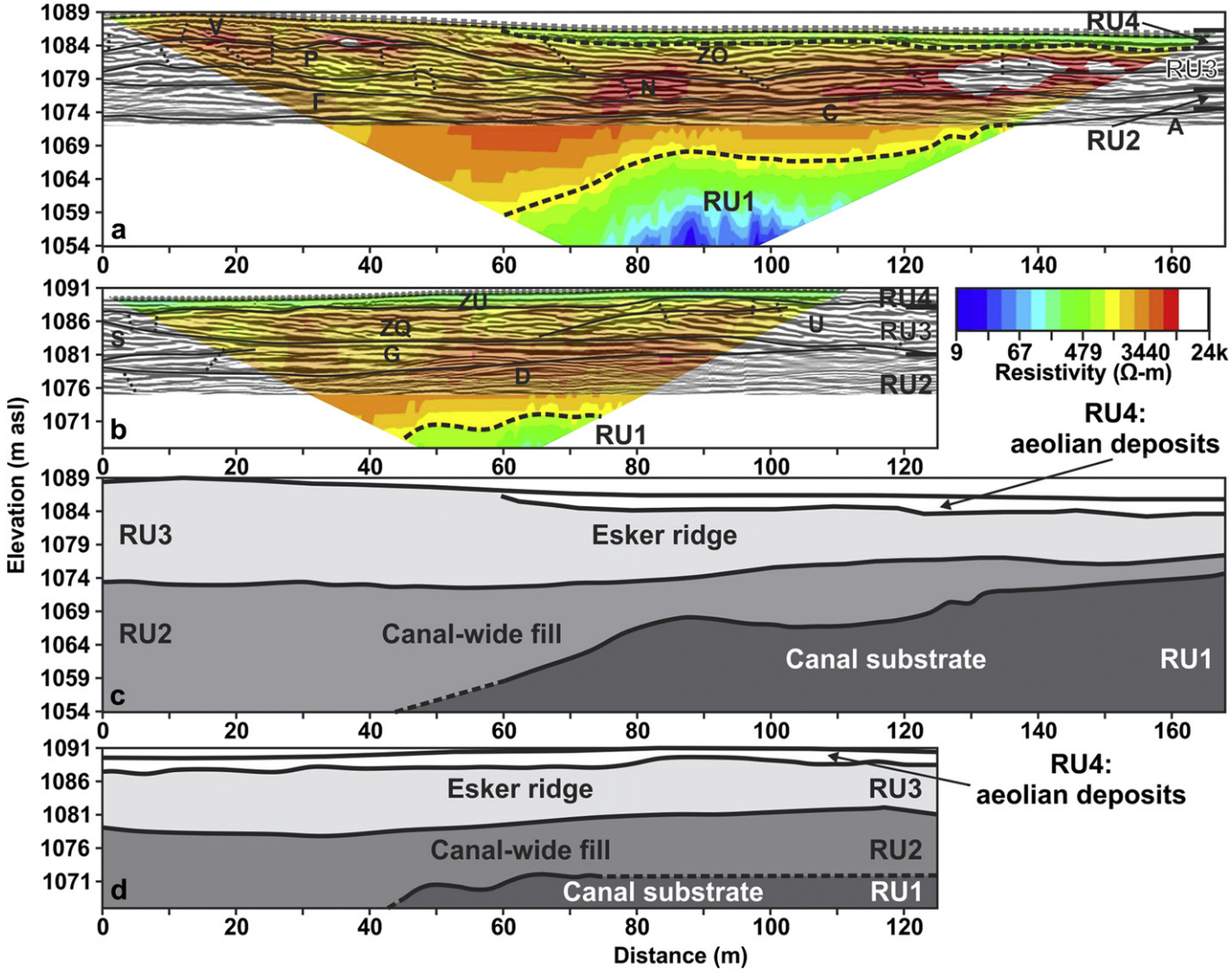

Fig. 11. Processed GPR and ERT profiles collected at lines a) X3 and b) X6 of grid 3. The data have been processed following the protocol described in Section 3.3. Inversion resulted in 8.9% (X3) and 3.7% (X6) data removal, RMS errors of 3.1% (X3) and 2.21% (X6), and l^2 values of 2.4 (X3) and 1.22 (X6). Lithostratigraphic resistivity units are labelled RU1–4. Radar element bounding surfaces are defined by the bold lines. The bounding surface of RU1 is indicated by the dashed lines, whereas those of RU2–4 follow radar element bounding surfaces (except for X3 where the bounding surface of RU4 is a dashed line because no bounding surface can be identified). Radar elements have been labelled in order of deposition. Short dotted lines mark offset reflections. Lithostratigraphic interpretations of ERT profiles collected at lines c) X3 and d) X6. Lithostratigraphic resistivity units are labelled RU1–4. The dashed lines mark inferred unit boundaries outside of the areas imaged by the GPR and ERT profiles. (For interpretation of the references to colour in this figure legend, the reader is referred to the web version of this article.)

those of RU3 at grids 1 and 2, are likely associated with a higher gravel content at grid 3, as observed on the landform surface (Fig. 4c vs. Fig. 4a, b). Low resistivity material (~300–700 Ω-m) at the landform surface form RU4, the location of which corresponds to that of localized fine sand observed at the esker ridge surface at lines X3 and X6.

Radar bounding surfaces delineate 47 radar elements (labelled A–Z and ZA–ZU on Figs. 11a, b and 12 and referred to as RE-A to RE-Z and RE-ZA to RE-ZU in the text). The stratigraphically deepest radar element, RE-A, is imaged wherever GPR penetration is great enough. Although its lower bounding surface is not imaged, the upper bounding surface of RE-A is defined by an often high amplitude continuous reflection, below which the GPR signal rapidly attenuates (independent of system electronics) (Figs. 11a and 12). RE-A can be traced discontinuously through the grid and because its stratigraphic position and elevation can be traced to RU1 (till) in the ERT profiles, RE-A defines the irregular (up to ~15 m of relief) canal base (Fig. 11). RE-B to RE-D are tabular elements that rest directly on the canal floor, often infilling topographic lows in the canal base (e.g., RE-B at ~310–610 m, line X1, Fig. 12). These radar elements are continuous across the full length of flow perpendicular lines (Y3 and Y12, Fig. 12), suggesting they extend beyond the width of the esker ridge. Although signal attenuation often prevents clear imaging of internal reflections, RE-B to RE-D are dominated by continuous subhorizontal reflections that onlap their lower bounding surface (where such reflections are visible e.g., ~1240–1350 m on line X1, Fig. 12). RE-C and RE-D correspond to RU2 in the ERT profiles and have a resistivity of up to ~7000 Ω-m (Fig. 11a, b). Because the stratigraphic position, vertical thickness, and internal characteristics of RE-B to RE-D are similar to RE-A (RU2) in grids 1 and 2 (Figs. 6 and 9), we interpret RE-B to RE-D at grid 3 as canal-wide fill (Table 1; Fig. 11c, d; stage 1, Fig. 13) similar to that reported by Burke et al. (2012). Thus, radar elements within RU3 (RE-E to RE-ZS, Figs. 11a, b and 12) lying above the canal-wide fill and within the esker ridge are interpreted as esker ridge sediments (Fig. 11c, d).

RE-E to RE-G record initial deposition within the esker-forming conduit and are ~100–210 m long and ~4–7 m thick. They have convex-up geometries, being tabular in flow-parallel lines and arched in flow-perpendicular lines (e.g., line Y2, Fig. 12). The lower bounding surface of RE-E is conformable to RE-A and interpreted as a paraconformity (non-depositional or erosional) (e.g., at ~200–300 m on line X1, Fig. 12), whereas those of RE-F and RE-G truncate reflections within RE-C and RE-D, respectively (e.g., at ~1240–1260 m on line X1, Fig. 12), suggesting they are erosional. Internal reflections onlap their lower bounding surfaces and are typically subhorizontal in flow-parallel lines (e.g., ~1070–1160 m on line X1) and slightly arched in flow-perpendicular lines (e.g., line Y2, Fig. 12). RE-E to RE-G record initial discontinuous vertical accretion (Table 1) of gravel sheets (cf. Wooldridge and Hickin, 2005) along an ice tunnel (stage 2, Fig. 13), similar to plane beds imaged by GPR in eskers elsewhere (e.g., Burke et al., 2010).

RE-H to RE-K are ~50–200 m long, >20 m wide, and ~3–6 m thick tabular (RE-H and RE-J) or convex-up, mound-like (RE-I and RE-K) radar elements. Their lower bounding surfaces truncate deeper reflections (e.g., at ~1480–1490 m on line X1, Fig. 12) and so are erosional. They are composed of continuous subplanar reflections that downlap or onlap the erosional lower bounding surfaces in flow-parallel (e.g., ~0–200 m and ~1410–1490 m of line X1, Fig. 12) and flow-perpendicular lines (line Y1, Fig. 12). RE-H to RE-K record vertical accretion of gravel sheets (stages 3–4, Fig. 13), upglacier from the initial depocentres defined by RE-E to RE-G (stage 2, Fig. 13). RE-L to RE-O are extensive (up to ~300 m long and 30 m wide) tabular radar elements, the lower bounding surfaces of which appear to be erosional, as they truncate deeper reflections (e.g., RE-N at ~1350–1375 m of line X1, Fig. 12). They are composed of continuous subhorizontal reflections that onlap or drape their lower bounding surface. RE-L to RE-N record continued vertical accretion of gravel sheets (stages 5–6, Fig. 13) downglacier (RE-L) and in between (RE-M and RE-O) the depocentres (stages 2–4, Fig. 13).

RE-P to RE-U are tabular, concave-up radar elements that are ~20–160 m long in flow-parallel lines, typically ridge wide in flow-perpendicular lines (~20 m), and ~3–10 m thick. These radar elements have lower bounding surfaces that truncate deeper reflections (erosional) (e.g., RE-R in line X1, Fig. 12) and are onlapped by the subparallel reflections that make up the radar elements (e.g., RE-U on line X6, Fig. 12). RE-P to RE-U record continued vertical accretion (Table 1) of gravel sheets at a depocentre corresponding to the location of the final ridge enlargement (stages 7–9, Fig. 13).

RE-V to RE-Y are upglacier stacked tabular elements ~100–150 m long, ridge-wide (up to at least 30 m), and ~3–6 m thick. RE-V to RE-X have lower bounding surfaces that truncate deeper reflections (erosional) and dip upflow at up to 10° (Fig. 12). These radar elements are dominated by reflections that also dip upflow (up to 15° dip) (e.g., RE-W at ~1050–1080 m on line X1, Fig. 12), recording headward accretion (Table 1; stages 10–13, Fig. 13) of gravel sheets (upflow of the ridge enlargement), similar to backset beds imaged by GPR in other eskers (e.g., Fiore et al., 2002; Burke et al., 2008, 2010). RE-Z to RE-ZB are vertically-stacked tabular elements up to ~290 m long, up to ~25 m wide, and ~3–6 m thick. Their lower bounding surfaces, which truncate deeper reflections (erosional) (e.g., at ~700–750 m of line X1, Fig. 12), are draped by continuous subhorizontal reflections and so record vertical accretion (Table 1) of gravel sheets (stages 14–16, Fig. 13) upglacier from the preceding radar elements (i.e., stage 13, Fig. 13). RE-ZC to RE-ZJ are broadly tabular ridge-wide elements up to 170 m long and 3–6 m thick. They have varied geometries and lower bounding surfaces that truncate deeper reflections and so are erosional (Fig. 12). RE-ZC, RE-ZF and RE-ZH have lower bounding surfaces dipping upglacier (~6–15° from horizontal) and are composed of continuous reflections that dip upflow at angles concordant to the lower bounding surfaces. RE-ZD, RE-ZE, RE-ZG, RE-ZI and RE-ZJ form either convex-up (RE-ZD and RE-ZE), concave-up (RE-ZG), or tabular (RE-ZI and RE-ZJ) radar elements that are composed of onlapping continuous subhorizontal reflections. RE-ZC to RE-ZJ are consistent with continued upglacier esker ridge growth through a combination of vertical and headward accretion (Table 1) of gravel sheets (cf. Wooldridge and Hickin, 2005) onto deeper radar elements (stages 17–22, Fig. 13).

RE-ZK to RE-ZQ are concave-up, trough-like elements that are up to ~160 m long, ridge wide, and ~3–5 m thick (Fig, 12). Their lower bounding surfaces truncate deeper reflections (erosional) and they are composed of onlapping subhorizontal reflections. RE-ZK to RE-ZQ record the final stages of deposition and their characteristics are consistent with discontinuous (along the esker-forming ice tunnel) vertical accretion of gravel sheets (stages 23–24, Fig. 13) similar to scour-and-fill (cf. Wooldridge and Hickin, 2005; Kostic and Aigner, 2007).

Offset reflections can be traced throughout all radar elements and whereas they are most common in flow-perpendicular lines, they also form closely-spaced clusters in flow-parallel lines (e.g., at ~1060–1100 m on line X1, Fig. 12). These clusters can be qualitatively correlated (positively) to the location of flanking kettle holes. Offsets in reflections can be continuously aligned for up to ~6 m (e.g., at ~12 m on line Y5, Fig. 12). Overall, these reflection offsets do not result in significant distortion of primary reflection geometry. Offset reflections are interpreted as faults associated with post-depositional slumping due to steep esker ridge flanks and

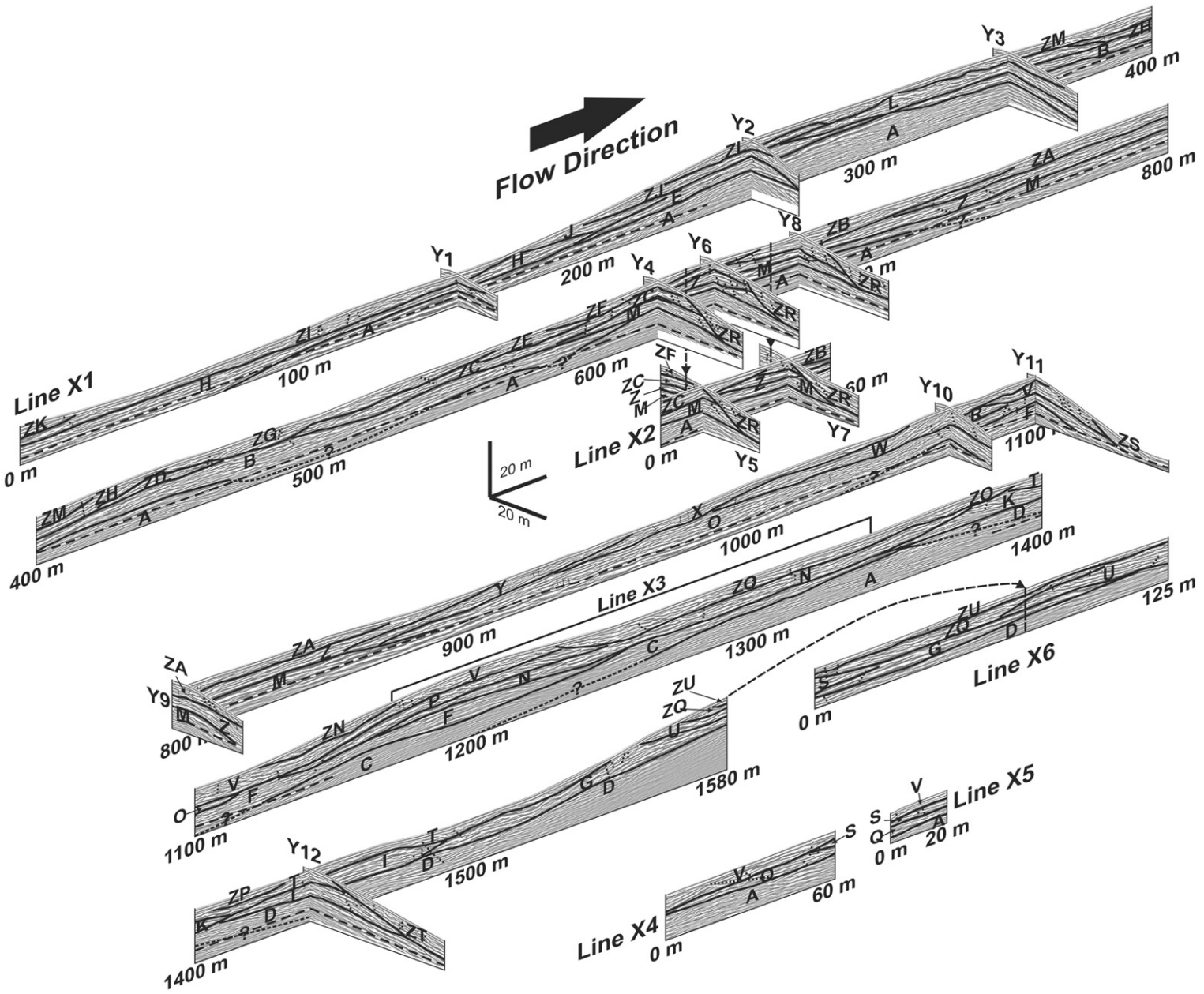

Fig. 12. Fence diagram of GPR profiles collected at grid 3. The data have been processed following the sequence described in Section 3.3. Line X1 is separated into five sections that can be identified by the hundred metre distance markers. True relative line orientations are shown in Fig. 1f. The location where line X3 coincides with X1 is indicated. Radar element bounding surfaces are defined by the bold lines. Where GPR signal attenuation has prevented continuous imaging of a bounding surface, inferred bounding surfaces are indicated by the short-dashed lines labelled '?'. The interpreted water table is defined by the wide dashed line. Radar elements have been labelled (A–Z and ZA–ZU) in order of deposition. Short dotted lines mark offset reflections.

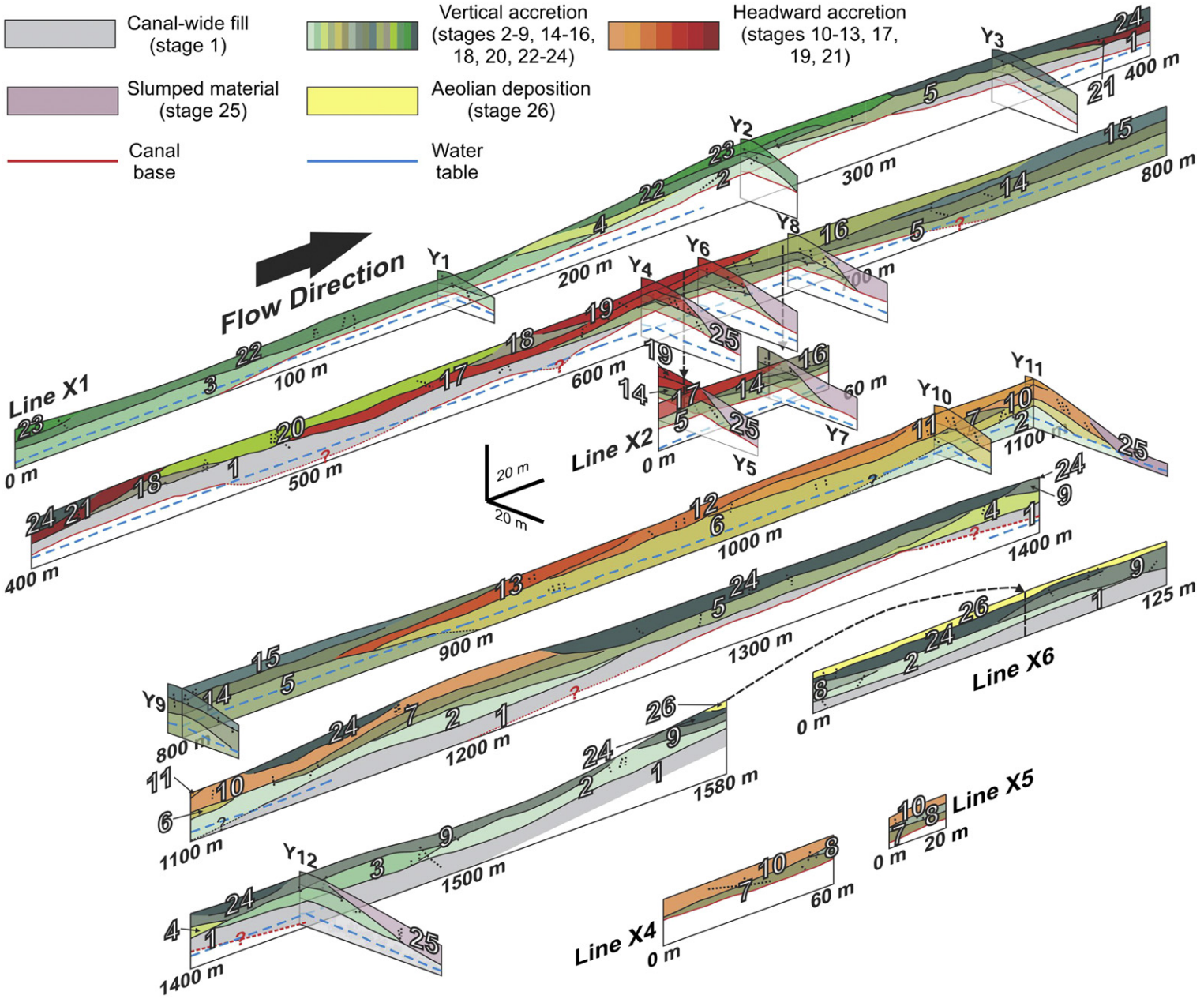

Fig. 13. Fence diagram of interpreted GPR profiles collected at grid 3. Line X1 is separated into five sections that can be identified by the hundred metre distance markers. True relative line orientations are shown in Fig. 1f. Radar elements have been colour-coded based upon the broad style of deposition, using the criteria outlined in Table 1. These colours correspond to those in legend (top left). The radar elements have been numbered (1–26) in order of deposition. Refer to animation 3 (see supplementary data) for an animation of depositional ordering. Short dotted lines mark faults. (For interpretation of the references to colour in this figure legend, the reader is referred to the web version of this article.)

removal (melting) of ice support (cf. Fiore et al., 2002; Burke et al., 2008, 2010; Woodward et al., 2008). RE-ZR to RE-ZT are only identified on flow-perpendicular lines (Fig. 12) and their positions correspond to steps in the esker ridge flank (Fig. 3e). They initiate close to offset reflections (e.g., at ~10–15 m on line Y6, Fig. 12), form asymmetrical troughs that increase in thickness away from the esker ridge crest, and are composed of discontinuous reflections distorted by offsets in reflections (e.g., RE-ZR on line Y4, Fig. 12). Because RE-ZR to RE-ZT initiate close to faults (offset reflections) within the esker ridge and lie below steps (treads) in the esker ridge cross-section, we interpret them as slumps (Table 1), resulting from collapse of the esker ridge flanks following removal (melting) of ice support.

The final stage of canal fill at grid 3 is recorded by RE-ZU (Fig. 12), which is poorly imaged due to the radar element lower bounding surface often being shallower than the area obscured by the GPR air- and ground-waves. The position of RE-ZU corresponds to RU4, which is a low resistivity (~400–700 Ω-m) unit at the landform surface (Fig. 11b). Because RU4 corresponds to the presence of fine sand at the esker ridge surface, and it has resistivity values similar to those reported for aeolian deposits elsewhere on the Fraser Plateau (Perkins et al., 2011b), we interpret RE-ZU as aeolian sediment (Table 1) deposited following esker ridge deposition (Fig. 11c, d; stage 26, Fig. 13). A similar aeolian unit is inferred at the surface of line X3 from the resistivity values, but this does not correspond to a radar element because its thickness is less than that of the airwave and groundwave (at 60–160 m on line X3, Fig. 11a).

In summary (animation 3; Fig. 11c, d), grid 3 records canal-wide fill (cf. Burke et al., 2012) that is largely located between high points in the irregular canal floor (till). Resting on this fill are extensive (several hundred metres long and ridge wide) esker ridge radar elements. Most esker ridge radar elements have a tabular geometry, and record vertical or headward accretion (Fig. 8a). However, depositional stages are typically separated by periods of erosion and so primary radar element geometry is no longer apparent. The stratigraphically-deepest esker ridge radar elements record discontinuous deposition in localized depocentres that are separated by areas of non-deposition or extensive erosion. Subsequent radar elements connect these depocentres through vertical accretion upglacier and downglacier from them, and the ridge enlargement at the downflow end of the grid is expanded through vertical gravel sheet accretion. Subsequent esker ridge deposition and landform development is in an upglacier direction via a combination of vertical and headward accretion. The presence of backset beds within some radar elements suggests flow conditions allowed the development of localized hydraulic jumps. The final stages of esker ridge deposition are recorded by disconnected, concave-up radar elements, the geometry and characteristics of which are consistent with scour-and-fill. The dominance of offset reflections in flow perpendicular lines indicates most post-depositional slumping was associated with removal (melting) of lateral ice support, consistent with the location of slumps along the esker ridge flanks. The clustering of faulting around flanking kettle holes is testament to the close association between the esker ridge and the ice blocks that formed the kettle holes. Following esker ridge formation, the landform was locally draped by aeolian sand.

5. Discussion

5.1. Synchronous or time-transgressive esker ridge formation?

The close proximity of the subaqueous fans (probably ice-contact due to minimal faulting) and the esker ridge raise the possibility of time-transgressive deposition of the esker ridge segments and fans (cf. Banerjee and McDonald, 1975; Brennand, 2000; Hooke and Fastook, 2007; Cummings et al., 2011). Because fan 2 is adjacent to a flat-topped esker ridge segment that was deposited subaerially, it is possible that flat-topped ridge segments and fans were deposited time-transgressively atop round-crested ridge segments (cf. Cummings et al., 2011). However, fans 1 and 3 are not adjacent to flat-topped esker ridge segments (fan 1 is adjacent to an esker ridge enlargement and fan 3 a round crested esker ridge segment) and no fan is adjacent to the flat topped ridge segment at grid 1 (Fig. 1c). We infer that all fans were deposited following, rather than during, esker ridge formation for seven reasons: 1) there is a mismatch in scale between the fans and the esker ridge (fans have small surface areas compared to esker ridge width and length); 2) fan surface elevations are >10 m lower than the esker ridge crest. Because the fan surfaces are not kettled and primary bedding within the fans is largely intact (i.e. not heavily faulted), it seems unlikely the fans were "let down" due to buried ice melt out; 3) fan morphology and sedimentology indicate complex flow directions oblique to, rather than parallel to the esker ridge crest, including flow towards, as well as away from the esker ridge; 4) the centrelines of fans 1 and 2 are consistent with the orientation of channels that cut perpendicularly through the esker ridge; 5) the fans do not drape the esker ridge, as might be expected if time-transgressive esker sedimentation had occurred (cf. Brennand, 2000; Hooke and Fastook, 2007), but rather sit adjacent to the esker ridge and are topographically constrained by it; 6) the esker ridge proper (RU3) is dominated by coarse sand and pebble- to cobble-gravel (Figs. 4a, d, 6c, 9b and 11c, d), whereas even in esker-proximal locations the fans are dominated by fine sand, silt, and clay (unit 1, Fig. 5b); and 7) fine material on the esker ridge surface, where present (RU4), is coarser than material making up the fan proper (Fig. 4d vs. unit 1, Fig. 5b) and instead has similar characteristics to unit 2 at the fan surface (Fig. 5b). These thin sand and silt carapaces are consistent with Holocene aeolian sediment (see Section 4.2) that is found extensively across the Fraser Plateau (cf. Lian and Huntley, 1999). Consequently, we do not consider the fans as part of the meltwater corridor landsystem *per se*, but rather part of a superimposed (later) proglacial lake landsystem. Rapid down and backwasting of the CIS on the Fraser Plateau resulted in proglacial lake formation (recorded by glaciolacustrine sediments in the area, cf. Tipper, 1971; Valentine and Schori, 1980) into which fine sediment (from the melting ice and reworking of previously deposited materials) was deposited. Thus, we envisage the esker ridge was deposited synchronously along its full length, as suggested by Burke et al. (2012).

5.2. Styles of esker ridge sedimentation

Although the esker ridge is not continuous for its full length, gaps between ridge sections are not associated with ice-marginal fans. Thus, the Chasm esker ridge was most likely deposited synchronously within an ice tunnel at least ~32 km in length. However, geophysical data reveal that changes in ridge morphology are associated with variation in the style of sedimentation.

5.2.1. Flat-topped esker ridge sedimentation (grids 1 and 2)

Deposition within grids 1 and 2 includes both canal-wide fill and esker ridge sediments. Initial esker ridge deposits at both grids, record localized deposition involving horizontally-extensive vertical accretion, with minor lateral, headward and downflow accretion. Depositional stages are separated by periods of erosion and so most elements no longer reflect their primary geometry. Such reworking is most prominent at grid 1 where radar elements

are relatively thin and have been truncated prior to the subsequent depositional phase. At grid 2, on the other hand, radar elements tend to be thicker, with internal reflection geometry suggesting the presence of large-scale, primary bedforms. At both grids this phase of alternating depositional and erosional stages is then replaced by periods of extensive (throughout the grid) vertical accretion that often infills topographic low points in the landform and results in the broad flat-topped ridge morphology. These flat-topped ridge morphologies are consistent with deposition in a channel with a free water surface (open channel) (cf. Russell et al., 2001). Because sediments at grids 1 and 2 form distinct ridges and contain faults suggesting the removal of lateral support, we interpret these flat-topped ridge segments to have been deposited within an ice-walled channel. Given the abrupt lithostratigraphic change in radar element characteristics, we suggest that esker ridge sedimentation initially took place in pressurised, subglacial ice tunnels that then unroofed during the final stages of esker ridge formation to become subaerial ice-walled channels. However, there are discrepancies between both the texture and architecture of subglacial ice tunnel deposits between grids 1 and 2. Radar elements at grid 1 tend to be thinner and separated by periods of more intense erosion than those at grid 2, which are thicker and include large-scale bedforms. These discrepancies suggest differences in flow depth and stream power (cf. Carling, 1999), as well as the possibility of reduced sediment supply at the time of esker ridge sediment deposition recorded at grid 1. Furthermore, the resistivity of ice tunnel deposits is lower at grid 1, suggesting a lesser gravel content. Consequently, sediments at grid 2 were likely deposited earlier (within the esker-forming event) than those at grid 1 when flow velocities were higher. This is probably because the ice tunnel at grid 2 unroofed before that at grid 1.

5.2.2. Round-crested, anbranched esker ridge and ridge enlargement (grid 3)

Deposition within grid 3 includes canal-wide fill followed by esker ridge sedimentation. Initial esker ridge deposition is irregular and includes laterally extensive, undulating units that conform to the substrate (till and canal-wide fill) long profile (Figs. 12 and 13). Initial radar elements form depocentres that are disconnected by non-deposition or erosion (stage 2, Fig. 13). Further vertical accretion is focussed at these depocentres, as well as upglacier and downglacier from them (stage 3–9, Fig. 13). Subsequent radar elements are stacked in an upglacier direction (stages 10–22, Fig. 13) suggesting an on-going and upglacier increase in accommodation space. This broad headward landform growth includes vertical and headward accretion resulting in macroform development (cf. Brennand, 1994). Backset beds (stages 10–13, 17, 19 and 21, Fig. 13) indicate the presence of hydraulic conditions consistent with abrupt channel enlargement and deposition similar to that in composite macroforms identified in other eskers (e.g., Brennand, 1994, 2000; Burke et al., 2008, 2010). The undulating esker ridge long profile suggests pressurised flow (closed-conduit flow) during esker ridge formation, which is consistent with the round-crested ridge morphology (Fig. 2) that also negates a free water surface because round-crested segments are composed of arched beds (cf. Garbutt, 1990) that indicate this is primary ridge morphology. Although faults within the landform and slump blocks along the esker ridge flanks are associated with removal of ice support (cf. Fiore et al., 2002; Woodward et al., 2008; Burke et al., 2008, 2010), GPR reflections within the landform are not highly distorted, further supporting subglacial esker ridge deposition (cf. Price, 1969; Banerjee and McDonald, 1975; Brennand, 2000). Consequently, esker ridge morphology, sedimentary architecture, and the limited presence of faulting indicate the ridge here was deposited in a pressurised, subglacial or low englacial ice tunnel (cf. Brennand, 1994, 2000). However, there is an increase in the frequency of faults and collapse within the vicinity of flanking kettle holes. This close association between the esker ridge and kettle holes suggests strong structural control on conduit location, which is consistent with increasing evidence from contemporary glaciers that conduits are generally controlled by glacial geologic structures (e.g., Fountain et al., 2005; Gulley and Benn, 2007; Benn et al., 2009; Gulley, 2009; Gulley et al., 2009) and similar inferences based on esker ridge and kettle hole patterns on the Canadian Shield (Craig, 1964).

Irregularities in radar element location, extent and geometry suggest spatial and temporal variation in accommodation space and sedimentation rate (cf. Brennand, 2000), likely linked to variations in conduit geometry (i.e. non-uniform ice tunnel geometry; e.g., Brennand, 1994; Fiore et al., 2002; Burke et al., 2008, 2010). The lack of fine material within ice tunnel deposits (Fig. 11), and presence of ridge-scale macroforms deposited within a conduit at least 20–30 m wide (based on radar element extent in flow-perpendicular lines) suggest rapid deposition similar to that reported from GLOF eskers (cf. Burke et al., 2010). Development of scour-and-fill elements during the final stage of esker ridge formation are likely associated with sediment reworking due to a reduced accommodation space (as the flow depth reduced due to filling of the ice tunnel with sediment) and/or changes in sediment supply.

5.3. Drainage system evolution

5.3.1. Glaciological and depositional setting

Although at LGM the CIS was ~600 m thick on the interior plateaus of BC (Huntley and Broster, 1994), we suggest ice over the meltwater corridor was probably <200 m thick at the time of esker ridge formation because: 1) the elevation difference between ice-marginal meltwater channels on the eastern slopes of the Marble Range (Fig. 1b) and the meltwater corridor base, suggests ice was <200 m thick over the meltwater corridor during final stages of the CIS here (Burke et al., 2012); 2) canal-wide fill does not display any evidence of the deformation that would be expected due to thick ice recoupling following the broad flow that eroded the canal and deposited the gravel sheets and dunes (Burke et al., 2012); 3) the canal-wide fill has not been reworked following deposition, suggesting the flow that deposited it was the last major event through the canal (Burke et al., 2012) and thus, during the final stages of the CIS; 4) the esker ridge is stratigraphically higher than the broad canal-wide fill and so was deposited later; and 5) the esker ridge was generated synchronously within a subglacial ice tunnel and, locally, an open ice-walled channel. Local open ice-walled channel flow requires the ice to be thin enough to allow ice tunnel unroofing.

The lack of reworking and burial by fines of the broad canal-wide fill underlying the Chasm esker ridge led Burke et al. (2012) to suggest that the late-waning stage of the GLOF flow responsible for canal-wide erosion and fill was focussed into a smaller ice tunnel recorded by the esker ridge. Such collapse of canal-forming (tunnel channel) flow into smaller ice tunnels has been previously inferred elsewhere (e.g., Shaw, 1983) and it is known that eskers can form during single GLOFs at contemporary glaciers (e.g., Burke et al., 2008, 2010). These eskers include clasts ripped-up from the glacier bed (cf. Russell et al., 2001), suggesting bed erosion took place prior to esker deposition. Our data from the Chasm esker ridge reveal that fine sediments are absent and ridge sedimentation is dominated by sand and gravel (Figs. 4a, c, 6c, 9b and 11c, d) that is arranged into ridge-scale macroforms deposited within a large ice

tunnel (at least 20–30 m wide). These observations are consistent with criteria suggested as diagnostic of GLOF deposition in eskers (cf. Burke et al., 2010) and so we suggest that the Chasm esker ridge was most likely generated on the waning stage of the GLOF that formed the canal here. This explains the lack of reworking and burial by fines of the canal-wide fill (Burke et al., 2012) and is also consistent with a general upward fining from the coarser, early-waning stage, canal-wide fill to the finer, late-waning stage, esker ridge sedimentation as recorded in the ERT profiles (Figs. 6c, 9b and 11a, b).

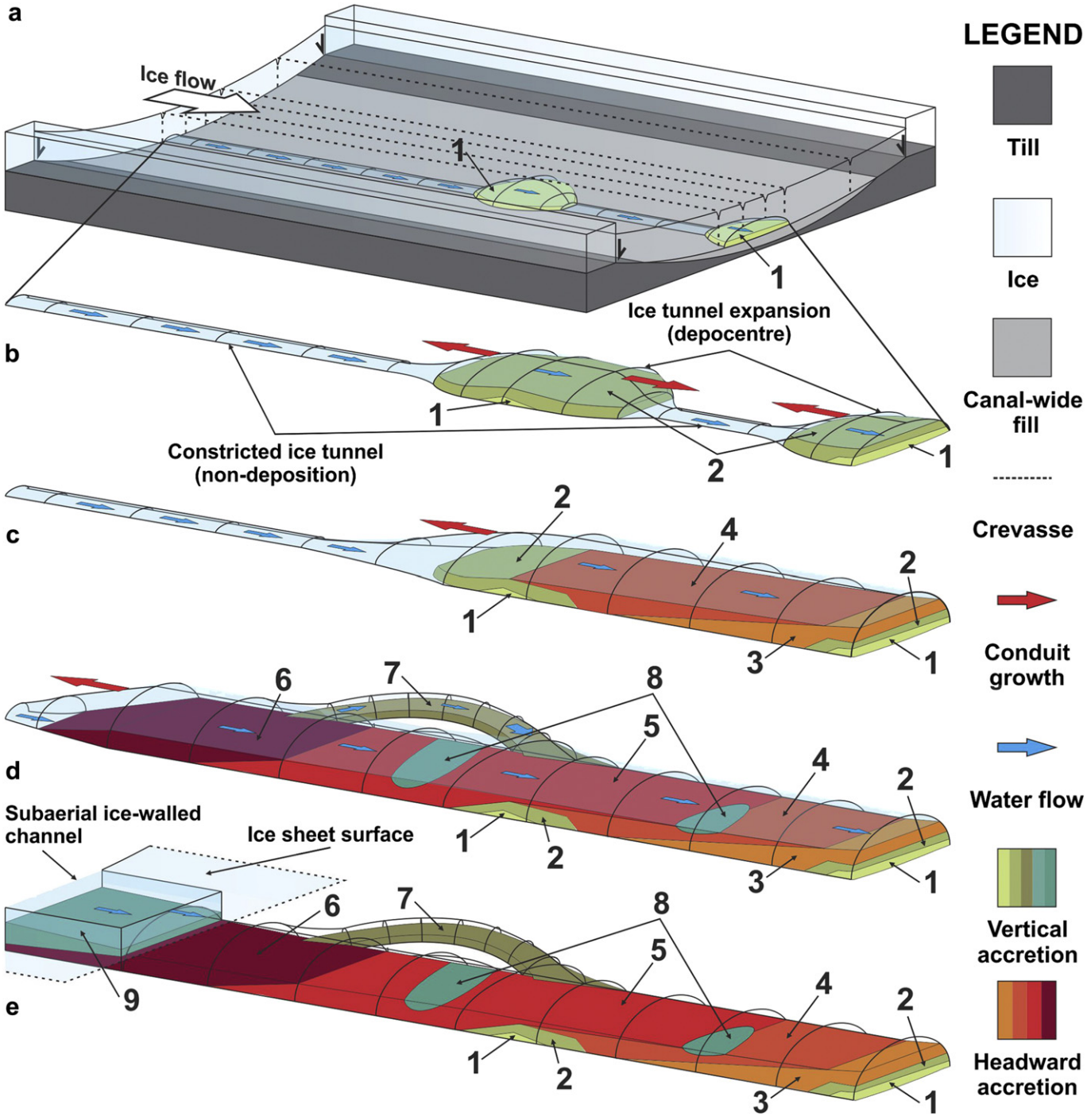

Fig. 14. Evolutionary model for ice tunnel development and Chasm esker formation on the southern Fraser Plateau, BC. a) The initial location of the irregular ice tunnel was controlled by structural weaknesses in the ice. The ice tunnel probably developed where the ice was heavily crevassed. Variations in ice tunnel geometry (accommodation space) resulted in depocentre development in ice tunnel expansions. These expansions were separated by non-deposition within ice tunnel constrictions. Panels b–e show enlarged views of this ice tunnel: b) Up- and down-glacier expansion of ice tunnel expansions resulted in associated esker segment growth. c) Upglacier ice tunnel growth connected the depocentres via headward deposition, resulting in esker segment growth in an upglacier direction. d) As the ice tunnel and esker grew in an upglacier direction, ice tunnel branches were developed where there were abundant structural weaknesses in the ice and this resulted in multi-thread esker segments. Ice tunnel infilling reduced accommodation space and resulted in reworking of earlier deposits. e) On the late waning stage, the thin overlying ice locally unroofed to form open channels. Here flat-topped esker segments accreted onto earlier ice tunnel deposits. Note that the model simplifies a complex depositional sequence and the presentation of depositional elements as flat-topped blocks does not reflect true esker morphology (except for element 9). Refer to text for further explanation. (For interpretation of the references to colour in this figure legend, the reader is referred to the web version of this article.)

5.3.2. Ice tunnel and esker ridge evolution

Initial canal-wide flow likely facilitated collapse and longitudinal crevasse formation along the GLOF path, similar to observations from contemporary GLOFs (Björnsson, 2002). It is likely that the late waning-stage flood path would have been initially controlled by these structural weaknesses in the ice (cf. Gulley and Benn, 2007; Benn et al., 2009; Gulley, 2009; Gulley et al., 2009). Along this flow path an efficient ice tunnel was then generated, with changes in esker ridge architecture recording spatial and temporal variation in ice tunnel geometry and accommodation space (cf. Brennand, 2000). Under the thin, inactive (cf. Fulton, 1991) ice conditions prevalent at the time of esker ridge formation, creep closure rates would have been low compared to thick ice scenarios, particularly over short timescales. Thus, the ice tunnel in which the Chasm esker ridge was deposited cannot be classified as an R-channel *senso stricto* because, by definition, an R-channel size is controlled by the balance between frictional melting of the ice walls and their creep closure (cf. Röthlisberger, 1972). Instead, the main factors (in addition to crevasse pattern) controlling ice tunnel geometry (accommodation space) would have been the balance between ice tunnel growth from frictional melting as well as mechanical excavation of the ice walls, and ice tunnel constriction from sediment deposition, rather than creep closure. Also, given only limited lateral accretion is identified within the esker ridge, most of the esker ridge does not appear to have formed within an H-channel (Hooke, 1984), which requires a gradual broadening of the ice tunnel. The architectural and morphological observations described in previous sections form the basis of an evolutionary model of ice tunnel development and esker ridge formation (Fig. 14).

During initial esker ridge sedimentation a continuous (to the glacier margin), but irregular (geometry) ice tunnel was developed along structural weaknesses in the ice. At this time local ice tunnel enlargements were separated by more constricted reaches (Fig. 14a). Variations in ice tunnel geometry were probably controlled by irregular ice surface collapse resulting from reductions in the integrity of the ice atop canal-wide flow. After canal-wide flow, the ice surface collapsed and local ice tunnel enlargement, enhanced by mechanical excavation of ice in areas of pervasive crevassing, resulted in an irregular ice tunnel geometry. Variation in accommodation space along the irregular ice tunnel facilitated development of local depocentres in ice tunnel expansions separated by non-deposition in ice tunnel constrictions (Fig. 14a, b). Sedimentation within these depocentres reduced accommodation space enhancing frictional melting and erosion of the ice tunnel walls. The resulting ice tunnel growth (Fig. 8b) around the depocentres increased accommodation space once more, facilitating further deposition within the expanding enlargements (Fig. 14b). General upglacier stacking of remaining esker ridge radar elements at grid 3 implies ice tunnel expansion upglacier from the depocentres (a form of paragenesis) (Fig. 14c). Continued upglacier expansion and headward accretion of radar elements generated obstacles to flow that then forced enlargement of constricted ice tunnel sections on the stoss side of depocentres, resulting in esker ridge deposition in an upglacier direction (Fig. 8b) and rapid ice tunnel infilling with gravel sheets and backset beds (macroforms) (Fig. 14d). Where the ice was highly crevassed floodwater was able to take advantage of multiple, structurally-controlled flow paths to form ice tunnel branches and deposit multi-thread esker ridge segments (of similar scale) separated by kettle holes. Where smaller, secondary esker ridge crests are not closely associated with kettle holes (Burke et al., 2012) these branches could have developed due to sediment infilling and blockage of the main ice tunnel (Aylsworth and Shilts, 1989). Ice tunnel infilling reduced accommodation space, resulting in local sediment reworking and development of scour-and-fill elements (Fig. 14d). Although the ice tunnel evolved in an overall upglacier direction (grid 3, Fig. 8b), this growth included vertical ice tunnel enlargement (Fig. 8b). Because the ice was thin, this vertical enlargement resulted in local ice tunnel unroofing to form open channel conditions. Here deposition beneath a free water surface resulted in broad accretion onto subglacial ice tunnel deposits and resulted in development of local flat-topped ridge segments (Fig. 14e). Because these flat-topped segments are composed of relatively fine sediment (resistivity values ~1000–4000 Ω-m in RU3 of Figs. 6c and 9b), have architectures more consistent with lower energy deposition (at least at grid 1), and are located towards the head of the esker ridge that was primarily developed through upglacier expansion of a continuous, but narrow ice tunnel, it is most likely they record the final stages of esker ridge formation.

6. Conclusions and wider implications

There is increasing evidence that many eskers record unsteadiness in dynamic glacial hydrologic systems (cf. Shulmeister, 1989; Brennand, 1994; Burke et al., 2008, 2010; Cummings et al., 2011), which is consistent with observations from contemporary ice masses (e.g., Bartholomaus et al., 2011). Our data from the southern Fraser Plateau suggest esker ridge deposition took place during a high-magnitude and probably single event (cf. Burke et al., 2010). The Chasm esker ridge most likely records the late waning stage of ice-dammed lake drainage following canal formation. Rapid ice tunnel development prevented reworking of canal-wide fill by focussing waning stage floodwater and sediment into the esker-forming ice tunnel. Preservation of the canal fill (broad deposits and esker ridge segments) implies that subsequent discharge of water through this canal must have been limited and so the canal landsystem must have been generated during the final stages of the CIS on the Fraser Plateau. Collapse of canal-forming flow into an esker-forming ice tunnel has been proposed as an explanation for preferential location of eskers in tunnel channels elsewhere (e.g., Shaw, 1983).

As the CIS was thin (cf. Huntley and Broster, 1994) and largely inactive (cf. Fulton, 1991) at the time of the Chasm esker ridge formation (Burke et al., 2012), our data reveal the processes operating during late-waning ice tunnel flow under these glaciological conditions. Although many field investigations of eskers invoke formation beneath thin, stagnant ice (e.g. Shilts, 1984; Aylsworth and Shilts, 1989; Dredge et al., 1999), studies that use esker patterns to verify numerical models (e.g. Boulton et al., 2009) or develop glacial hydrological theory (e.g., Shreve, 1985; Clark and Walder, 1994; Hooke and Fastook, 2007) often assume conduit geometry was governed by the balance between conduit growth from frictional melting and closure due to ice creep. However, such assumptions require the presence of thick, active ice at the time of esker formation and cannot be applied to short-lived hydrological events beneath thin, inactive ice. The final stages of the CIS on the Fraser Plateau would not be conducive to conduit squeezing (from creep closure) being the dominant factor that controlled reductions in conduit cross-sectional area. Consequently, the factors required for R-channel formation were not present at the time of formation of the Chasm esker ridge on the Fraser Plateau and this is reflected in esker ridge architecture and landform associations. During meltwater corridor landsystem development, reductions in flood stage were followed by ice surface collapse along the flow path, facilitating pervasive crevassing. Because the ice was thin, these crevasses then provided structural weaknesses along which waning flow was focussed and an esker-forming ice tunnel was developed. Such strong structural control is documented by the close association of esker ridge segments and kettle holes and is

consistent with increasing evidence that englacial conduits at contemporary glaciers are controlled by antecedent structures in the ice (e.g., Fountain et al., 2005; Gulley and Benn, 2007; Benn et al., 2009; Burke et al., 2009; Gulley, 2009; Gulley et al., 2009). This initial structurally-controlled channel then evolved from a continuous, but inefficient ice tunnel (due to a highly irregular geometry governed by crevasse pattern) into a more efficient ice tunnel.

The Chasm esker ridge sedimentary architecture and landform associations reveal that eskers may record unsteadiness in the glacial hydrologic system. During ice tunnel development, reduction in conduit cross-sectional area was determined by the sedimentation rate relative to conduit enlargement by frictional melting and mechanical ice excavation. The balance between these governing factors resulted in the dynamic changes in accommodation space (conduit geometry) that were fundamental to esker ridge formation, as reflected in the complex esker ridge sedimentary architecture. Consequently, the primary factors controlling formation of the Chasm esker ridge were the interaction between conduit geometry (accommodation space), flow conditions, and sediment supply. This is consistent with the inferred controls on GLOF esker formation at contemporary glaciers (Burke et al., 2010).

Within the Chasm esker, ridge cross-sectional area is closely related to the presence of macroforms that in turn are linked to changes in ice tunnel geometry during esker ridge deposition (cf. Brennand, 1994, 2000; Delaney, 2001; Fiore et al., 2002; Burke et al., 2008, 2010). Composite macroforms, which have characteristic backset to foreset bed transitions, probably require the sudden generation of a conduit enlargement to initiate backset deposition and then rapid sedimentation that generates a flow separation and foreset progradation downflow from the backsets (cf. Brennand, 1994). Composite macroforms are thought to be diagnostic of GLOF deposition (cf. Burke et al., 2010). Ridge-scale units of backset beds are identified within the Chasm esker ridge, which, given our interpretation that the esker ridge was generated on the waning stage of a high-magnitude GLOF, support the argument that composite macroforms are indeed diagnostic of GLOFs through esker-forming ice tunnels (cf. Burke et al., 2010). However, these backset beds are not associated with foreset progradation, indicating a lee-side flow separation was not generated. Although more testing is necessary, the lack of a lee-side flow separation is probably due to a lower sedimentation rate and/or flow power during formation of the Chasm esker ridge than that during contemporary GLOF esker formation reported by Burke et al. (2010). Furthermore, the Chasm esker ridge texture was dictated by sediment supply constraints, similar to those reported by Burke et al. (2010). Although boulders are present within the canal fill (Fig. 4e, f), indicating the flow had the competence to transport them, they are rare within the esker ridge itself (Fig. 4a–c) suggesting that flow powers in esker-forming flows were insufficient to transport boulders.

Our data imply that variation in esker ridge morphology can be used, in part, to make genetic interpretations of esker ridge formation. Round-crested, undulating ridge segments may record deposition in pressurised subglacial ice tunnels, whereas flat-topped ridge segments may record deposition during open channel (free water surface) flow due to subglacial ice tunnel unroofing. However, where an ice tunnel unroofs the sediment that results in a flat-topped morphological expression may only account for some of the sediment within the ridge segment, as ice tunnel deposits can be found at depth due to earlier subglacial deposition. Many flat-topped eskers have been identified on the Canadian Shield (e.g., St. Onge, 1984; Shilts et al., 1987) where they are typically linked to subaerial deposition close to the ice margin. Although subaqueous fans were identified adjacent to the Chasm esker ridge, these were formed after synchronous esker ridge formation and so the presence of subaqueous fans, even when close to flat-topped segments, need not imply time-transgressive esker formation. Furthermore, we identify no correlation between canal floor topography and esker ridge morphology (Fig. 2b), as suggested by Shreve (1985). Instead, variations in esker ridge morphology are controlled by hydrological and glaciological configurations that are independent of basal topography. These data demonstrate that landform mapping alone is not sufficient to constrain the dynamism that may take place within an esker-forming ice tunnel. Only through a combination of landform mapping and sedimentary architecture data, can the specific factors responsible for ice tunnel evolution be identified. Because esker morphology and distribution have been used to test numerical ice sheet models (e.g., Boulton et al., 2009) and numerical models have been used to explain esker patterns (e.g., Hooke and Fastook, 2007), it is vital that the underlying assumptions used in numerical models are consistent with the landform record. On the Fraser Plateau the canal landsystem was, at least in part, controlled by an antecedent drainage network (cf. Burke et al., 2012), yet the canal fill (geomorphic signature) records high-magnitude flood flow, rather than sedimentation in a long-term antecedent drainage network. It is imperative that a better understanding of the interaction between antecedent drainage networks and transient water inputs is gained in order to improve constraints on numerical models of the subglacial hydrologic system. It is likely that many of the assumptions currently used in numerical models of ice sheet subglacial hydrology may not be applicable to transient subglacial environments.

Acknowledgements

This work was supported by a scholarship to MJB from The Leverhulme Trust, an NSERC Discovery grant and equipment grants to TAB, and a GSA Student Research Grant to AJP. We are grateful to John Woodward and Northumbria University for loan of their GPR, and thank Jared Peters for assistance in the field. We also thank David Sharpe and Donald Cummings for detailed comments that have significantly improved the manuscript.

Appendix A. Supplementary data

Supplementary data (GPR data and interpretations presented two-dimensionally, as well as animations 1–3) related to this article can be found at http://dx.doi.org/10.1016/j.quascirev.2012.09.004.

References

Arcone, S.A., Lawson, D.E., Delaney, A.J., 1995. Short-pulse radar wavelet recovery and resolution of dielectric contrasts within englacial and basal ice of Matanuska Glacier, Alaska, U.S.A. Journal of Glaciology 41 (137), 68–86.

Aylsworth, J.M., Shilts, W.W., 1989. Glacial Features Around the Keewatin Ice Divide, Districts of Mackenzie and Keewatin. In: Geological Survey of Canada Paper 88–24, 21 pp.

Banerjee, I., McDonald, B.C., 1975. Nature of esker sedimentation. In: Jopling, A.V., McDonald, B.C. (Eds.), Glaciofluvial and Glaciolacustrine Sedimentation. Society of Economic Palaeonologists and Mineralogists. Special Publication, vol. 23, pp. 304–320.

Bartholomaus, T.C., Anderson, R.S., Anderson, S.P., 2011. Growth and collapse of the distributed subglacial hydrologic system of Kennicott Glacier, Alaska, USA, and its effects on basal motion. Journal of Glaciology 57 (206), 985–1002.

Bell, R.E., 2008. The role of subglacial water in ice sheet mass balance. Nature Geoscience 1, 297–304.

Benn, D.I., Gulley, J.D., Luckman, A., Adamek, A., Glowacki, P.S., 2009. Englacial drainage systems formed by hydrologically driven crevasse propagation. Journal of Glaciology 55 (191), 513–523.

Bingham, R., Nienow, P., Sharp, M., Boon, S., 2005. Subglacial drainage processes at a High Arctic polythermal valley glacier. Journal of Glaciology 51, 15–24.

Björnsson, H., 2002. Subglacial lakes and GLOFs in Iceland. Global and Planetary Change 35, 255–271.

Booth, D.B., Troost, K.G., Clague, J.J., Waitt, R.B., 2003. The Cordilleran Ice Sheet. Developments in Quaternary Science 1, 17–43.

Boulton, G.S., Lunn, R., Vidstrand, P., Zatsepin, S., 2007a. Subglacial drainage by groundwater-channel coupling, and the origin of esker systems: part 1 – glaciological observations. Quaternary Science Reviews 26, 1067–1090.
Boulton, G.S., Lunn, R., Vidstrand, P., Zatsepin, S., 2007b. Subglacial drainage by groundwater-channel coupling, and the origin of esker systems: part II – theory and simulation of a modern system. Quaternary Science Reviews 26, 1091–1105.
Boulton, G.S., Hagdorn, M., Maillot, P.B., Zatsepin, S., 2009. Drainage beneath ice sheets: groundwater-channel coupling, and the origin of esker systems from former ice sheets. Quaternary Science Reviews 28, 621–638.
Brennand, T.A., Shaw, J., 1996. The Harricana glaciofluvial complex, Abiti region, Quebec: its genesis and implications for meltwater regime and ice-sheet dynamics. Sedimentary Geology 102, 221–262.
Brennand, T.A., 1994. Macroforms, large bedforms and rhythmic sedimentary sequences in subglacial eskers, south-central Ontario: implications for esker genesis and meltwater regime. Sedimentary Geology 91, 9–55.
Brennand, T.A., 2000. Deglacial meltwater drainage and glaciodynamics: inferences from Laurentide eskers, Canada. Geomorphology 32, 263–293.
Burke, M.J., Woodward, J., Russell, A.J., Fleisher, P.J., Bailey, P.K., 2008. Controls on the sedimentary architecture of a single event englacial esker: Skeiðarárjökull, Iceland. Quaternary Science Reviews 27, 1829–1847.
Burke, M.J., Woodward, J., Russell, A.J., Fleisher, P.J., 2009. Structural controls on englacial esker sedimentation: Skeiðarárjökull, Iceland. Annals of Glaciology 50 (51), 85–92.
Burke, M.J., Woodward, J., Russell, A.J., Fleisher, P.J., Bailey, P.K., 2010. The sedimentary architecture of outburst flood eskers: a comparison of ground-penetrating radar data from Bering Glacier, Alaska and Skeiðarárjökull, Iceland. Geological Society of America Bulletin 122, 1637–1645.
Burke, M.J., Brennand, T.A., Perkins, A.J., 2012. Evolution of the subglacial hydrologic system beneath the rapidly decaying Cordilleran Ice Sheet caused by ice-dammed lake drainage: implications for meltwater-induced ice acceleration. Quaternary Science Reviews 50, 125–140.
Carling, P.A., 1999. Subaqueous gravel dunes. Journal of Sedimentary Research 69 (3), 534–545.
Carter, S.P., Blankenship, D.D., Young, D.A., Peters, M.E., Holt, J.W., Siegert, M.J., 2009. Dynamic distributed drainage implied by the flow evolution of the 1996–1998 Adventure Trench subglacial lake discharge. Earth and Planetary Science Letters 283, 24–37.
Clague, J.J., James, T.S., 2002. History and isostatic effects of the last ice sheet in southern British Columbia. Quaternary Science Reviews 21, 71–87.
Clark, P.U., Walder, J.S., 1994. Subglacial drainage, eskers, and deforming beds beneath the Laurentide and Eurasian ice sheets. Geological Society of America Bulletin 106, 304–314.
Colgan, W., Rajaram, H., Anderson, R., Steffen, K., Phillips, T., Joughin, I., Zwally, H.J., Abdalati, W., 2011. The annual glaciohydrology cycle in the ablation zone of the Greenland ice sheet: part 1. hydrology model. Journal of Glaciology 57 (204), 697–709.
Craig, B.G., 1964. Surficial Geology of East-Central District of Mackenzie. Geological Survey of Canada, Bulletin 99, 23.
Cummings, D.I., Gorrell, G., Guilbault, J.-P., Hunter, J.A., Logan, C., Ponomarenko, D., Pugin, A.J.-M., Pullan, S.E., Russell, H.A.J., Sharpe, D.R., 2011. Sequence stratigraphy of a glaciated basin fill, with a focus on esker sedimentation. Geological Society of America Bulletin 123 (7–8), 1478–1496.
Delaney, C., 2001. Esker formation and the nature of deglaciation: the Ballymohon esker, Central Ireland. North West Geography 1 (2), 23–33.
Dredge, L.A., Kerr, D.E., Wolfe, S.A., 1999. Surficial materials and related ground ice conditions, Slave Province, N.W.T., Canada. Canadian Journal of Earth Sciences 36, 1227–1238.
Fay, H., 2002. Formation of kettle holes following a glacial outburst flood (jökulhlaup) Skeiðarársandur, southern Iceland. In: Snorrason, Á. (Ed.), Extremes of the Extremes: Extraordinary Floods. Proceedings of a Symposium Held in Reykjavik, July 2000. International Association of Hydrological Sciences Special Publication, vol. 271, pp. 205–210.
Fiore, J., Pugin, A., Beres, M., 2002. Sedimentological and GPR studies of subglacial deposits in the Joux Valley (Vaud, Switzerland): backset accretion in an esker followed by an erosive GLOF. Géographie physique et Quaternaire 56 (1), 19–32.
Flowers, G.E., Clarke, G.K.C., 2002. A multicomponent model of glacier hydrology 1. Theory and synthetic examples. Journal of Geophysical Research 107. http://dx.doi.org/10.1029/2001JB001122.
Fountain, A.G., Jacobel, R.W., Schlichting, R., Jansson, P., 2005. Fractures as the main pathways of water flow in temperate glaciers. Nature 433, 618–621.
Fricker, H.A., Scambos, T., 2009. Connected subglacial lake activity on lower Mercer and Whillans Ice Streams, West Antarctica, 2003–2008. Journal of Glaciology 55 (190), 303–315.
Fricker, H.A., Scambos, T., Bindschadler, R., Padman, L., 2007. An active subglacial water system in West Antarctica mapped from space. Science 315, 1544–1548.
Fulton, R.J., 1991. A conceptual model for the growth and decay of the Cordilleran Ice Sheet. Géographie physique et Quaternaire 45 (3), 281–286.
Garbutt, M.D., 1990. Full and Open Conduit Sedimentation Within a Large-Scale Esker System in Southwestern Finland. Geological Society of America, North Eastern Sections, Program with Abstracts 22, 19 pp.
Gray, L., Joughin, I., Tulaczyk, S., Spikes, V.B., Bundschadler, R., Jezek, K., 2005. Evidence for subglacial water transport in the West Antarctic Ice Sheet through three-dimensional satellite radar interferometry. Geophysical Research Letters 32, L03501.
Gulley, J., Benn, D.I., 2007. Structural control of englacial drainage systems in Himalayan debris-covered glaciers. Journal of Glaciology 53 (182), 399–412.
Gulley, J.D., Benn, D.I., Screaton, E., Martin, J., 2009. Mechanisms of englacial conduit formation and their implications for subglacial recharge. Quaternary Science Reviews 28, 1984–1999.
Gulley, J., 2009. Structural control of englacial conduits in the temperate Matanuska Glacier, Alaska, USA. Journal of Glaciology 55 (192), 681–690.
Hebrand, M., Åmark, M., 1989. Esker formation and glacier dynamics in eastern Skåne and adjacent areas, southern Sweden. Boreas 18, 67–81.
Heinz, J., Aigner, T., 2003. Three-dimensional GPR analysis of various Quaternary gravel-bed braided river deposits (southwestern Germany). In: Bristow, C.S., Jol, H.M. (Eds.), Ground-penetrating Radar in Sediments. Geological Society, London, Special Publications, vol. 211, pp. 99–110.
Hooke, R.LeB., Fastook, J., 2007. Thermal conditions at the bed of the Laurentide ice sheet in Maine during deglaciation: implications for esker formation. Journal of Glaciology 53 (183), 646–658.
Hooke, R.LeB., 1984. On the role of mechanical energy in maintaining subglacial water conduits at atmospheric pressure. Journal of Glaciology 30 (105), 180–187.
Huddart, D., Bennett, M.R., Glasser, N.F., 1999. Morphology and sedimentology of a high arctic eskers system: Vegbreen, Svalbard. Boreas 28, 253–273.
Huntley, D.H., Broster, B.E., 1994. Glacial Lake Camelsfoot: a Late Wisconsinan advance stage proglacial lake in the Fraser River Valley, Gang Ranch area, British Columbia. Canadian Journal of Earth Sciences 31, 798–807.
Jordan, T.A., Ferraccioli, F., Corr, H., Graham, A., Armadillo, E., Bozzo, E., 2010. Hypothesis for mega-outburst flooding from a palaeo-subglacial lake beneath the East Antarctic Ice Sheet. Terra Nova 22, 283–289.
Kostic, B., Aigner, T., 2007. Sedimentary architecture and 3D ground-penetrating radar analysis of gravelly meandering river deposits (Neckar Valley, SW Germany). Sedimentology 54, 789–808.
Lian, O.B., Huntley, D.J., 1999. Optical dating studies of postglacial aeolian deposits from the south-central interior of British Columbia, Canada. Quaternary Science Reviews 18, 1453–1466.
Mäkinen, J., 2003. Time-transgressive deposits of repeated depositional sequences within interlobate glaciofluvial (esker) sediments in Köyliö, SW Finland. Sedimentology 50, 327–360.
Ng, F.S.L., 2000. Canals under sediment-based ice sheets. Annals of Glaciology 30, 146–152.
Nienow, P., Sharp, M., Willis, I., 1998. Dye tracer investigations at the Haut Glacier d'Arolla, Switzerland: the late-summer configuration of the subglacial drainage system. Earth Surface Processes and Landforms 22, 825–843.
Palmer, S., Shepherd, A., Nienow, P., Joughin, I., 2011. Seasonal speed up of the Greenland Ice Sheet linked to routing of surface water. Earth and Planetary Science Letters 302, 423–428.
Pellicer, X.M., Gibson, P., 2011. Electrical resistivity and ground penetrating radar for the characterisation of the internal architecture of Quaternary sediments in the Midlands of Ireland. Journal of Applied Geophysics 75, 638–647.
Perkins, A.J., Brennand, T.A., Burke, M.J., 2011a. Esker Formation and Meltwater Routing on and Beneath the Margins of the Last Cordilleran Ice Sheet: Implications for Modelling Ice Sheet Hydrology. Abstract C11E-0717 Presented at 2011 Fall Meeting, AGU, San Francisco, California, 5–9 December.
Perkins, A.J., Brennand, T.A., Burke, M.J., 2011b. The genesis of an esker-like ridge at the margins of the last Cordilleran Ice Sheet. In: Proceedings of Geohydro2011, Quebec City August 28th–31st.
Pimentel, S., Flowers, G.E., 2010. A numerical study of hydrologically driven glacier dynamics and subglacial flooding. Proceedings of the Royal Society A. http://dx.doi.org/10.1098/rspa.2010.0211.
Plouffe, A., Bednarski, J.M., Huscroft, C.A., Anderson, R.G., McCuaig, S.J., 2011. Late Wisconsinan glacial history in the Bonaparte Lake map area, south-central British Columbia: implications for glacial transport and mineral exploration. Canadian Journal of Earth Sciences 48, 1091–1111.
Price, R.J., 1969. Moraines, sandur, kames and eskers near Breiðamerkurjökull, Iceland. Transactions of the Institute of British Geographers 46, 17–43.
Province of British Columbia, 2010. 1 Metre Resolution Black and White Orthophoto Mosaic (92Psw), 1:20,000. Open Government Licence for Government of BC Information, vBC1.0.
Röthlisberger, H., 1972. Water pressure in intra- and sub-glacial channels. Journal of Glaciology 11, 177–203.
Russell, A.J., Knudsen, Ó., Fay, H., Marren, P.M., Heinz, J., Tronicke, J., 2001. Morphology and sedimentology of a giant supraglacial, ice-walled, GLOF channel Skeiðarárjökull, Iceland: implications for esker genesis. Global and Planetary Change 28, 193–216.
Samouëlian, A., Cousin, I., Tabbagh, A., Bruand, A., Richard, G., 2005. Electrical resistivity survey in soil science: a review. Soil & Tillage Research 83, 173–193.
Shaw, J., 1983. Drumlin formation related to inverted melt-water erosional marks. Journal of Glaciology 29 (103), 461–479.
Shilts, W.W., Aylsworth, J.M., Kaszycki, C.A., Klassen, R.A., 1987. Canadian shield. In: Graf, W.L. (Ed.), Geomorphic Systems of North America. GSA Centenial Special, vol. 2, pp. 119–150.
Shilts, W.W., 1984. Esker Sedimentation Models, Deep Rose Lake Map Area, District of Keewatin. In: Geological Survey of Canada, Current Research 84-1B, pp. 217–222.
Shreve, R.L., 1985. Esker characteristics in terms of glacier physics, Katahdin esker system, Maine. Geological Society of America Bulletin 96, 639–646.
Shulmeister, J., 1989. Flood deposits in the Tweed Esker (southern Ontario, Canada). Sedimentary Geology 65, 153–163.

Sole, A.J., Mair, D.W.F., Nienow, P.W., Bartholemew, I.D., King, M.A., Burke, M.J., Joughin, I., 2011. Seasonal speed-up of a Greenland marine-terminating outlet glacier forced by surface melt-induced changes in subglacial hydrology. Journal of Geophysical Research 116, F03014.

St. Onge, D.A., 1984. Surficial Deposits of the Redrock Lake Area, District of Mackenzie. In: Geological Survey of Canada, Current Research 84-1a, pp. 271–277.

Stearns, L.A., Smith, B.E., Hamilton, G.S., 2008. Increased flow speed on a large East Antarctic outlet glacier caused by subglacial floods. Nature Geoscience 1, 827–831.

Tipper, H.W., 1971. Multiple glaciation in central British Columbia. Canadian Journal of Earth Sciences 8, 743–752.

Valentine, K.W.G., Schori, A., 1980. Soils of the Lac La Hache – Clinton Area, British Columbia. In: British Columbia Soil Survey 25. Research Branch, Agriculture Canada, 118 pp.

Walder, J.S., Fowler, A., 1994. Channelized subglacial drainage over a deformable bed. Journal of Glaciology 40 (134), 3–15.

Werder, M.A., Loye, A., Funk, M., 2009. Dye tracing a jökulhlaup: I. Subglacial water transit speed and water-storage mechanism. Journal of Glaciology 55 (193), 889–898.

Wingham, D.J., Siegert, M.J., Shepherd, A., Muir, A.S., 2006. Rapid discharge connects Antarctic subglacial lakes. Nature 440, 1033–1036.

Winsemann, J., Asprion, U., Meyer, T., Schramm, C., 2007. Facies characteristics of Middle Pleistocene (Saalian) ice-margin subaqueuous fan and delta deposits, glacial lake Leine, NW Germany. Sedimentary Geology 193, 105–129.

Woodward, J., Burke, M.J., Tinsley, R., Russell, A.J., 2008. Investigating reworking of proglacial sediments using GPR: Skeiðarárjökull, Iceland. In: Rodgers, C.D.F., Chignell, R.J. (Eds.), Proceedings of the 12th International Conference on Ground Penetrating Radar. University of Birmingham, Birmingham.

Wooldridge, C.L., Hickin, E.J., 2005. Radar architecture and evolution in wandering gravel-bed rivers: Fraser and Squamish Rivers, British Columbia, Canada. Journal of Sedimentary Research 75, 844–860.